# Representing rectangular jet dynamics through azimuthal Fourier modes

Surya Chakrabarti, Datta Gaitonde, and S. Unnikrishnan

Phys. Rev. Fluids **6**, 074605 — Published 8 July 2021

DOI: 10.1103/PhysRevFluids.6.074605

# Representing Rectangular Jet Dynamics Through Azimuthal Fourier Modes

Surya Chakrabarti[*] and Datta Gaitonde[†]
*Mechanical and Aerospace Engineering,*
*The Ohio State University,*
*Columbus, Ohio, 43210*

S. Unnikrishnan[‡]
*Florida Center for Advanced Aero-Propulsion (FCAAP), FAMU-FSU College of Engineering,*
*The Florida Sate University, Tallahassee, Florida, 32310*

(Dated: June 17, 2021)

Rectangular propulsion nozzles offer thrust-vectoring and air-frame-integration advantages over their more commonly studied circular counterparts. However, they display many distinguishing features which violate assumptions, such as azimuthal homogeneity, typically used in prediction tools for circular jets. In the present work, we examine the utility of an azimuthal Fourier decomposition for rectangular Mach 1.3 jets of aspect ratios (AR) 1, 4 and 8 using Large-Eddy Simulations, with a circular jet of same equivalent diameter for reference. The simulations manifest key features of rectangular jets, including higher spreading rates and shorter potential cores with increasing AR, axis switching (AR=4) and azimuthal variation in peak acoustic intensity (AR=8). We show that, after projection on a cylindrical frame, a sine-cosine ansatz for the azimuthal Fourier series affords a more convenient representation of non-axisymmetric flow features than the commonly used complex exponential ansatz. Fluctuation magnitudes of the higher azimuthal modes show rapid reduction in amplitude, similar to those observed in circular jets, especially if an acoustic fluctuation field based on momentum potential theory is chosen instead of pressure fluctuations. The leading modes differ, however, from those of a circular jet in two important aspects, namely, the mechanisms represented by the sine and cosine coefficients of the first azimuthal mode and the rate of streamwise decay of all modes with increasing AR. These differences are traced to the near and farfield rectangular jet asymmetry by examining azimuthal inhomogeneity, whose implications are assessed with a generalized expression for acoustic intensity based on energies of leading modes. The significant simplicity of circular plumes is recovered as a special case of the analysis. Invocation of the two-fold mirror symmetry property of rectangular jets eases the prediction procedure so that only two extra terms, representing mechanisms unique to rectangular jets, specifically preferential flapping in the minor axis direction and coupling of axisymmetric and second azimuthal modes, are sufficient to recover the advantages of azimuthal decomposition.

## I. INTRODUCTION

Increasing engine power requirements for commercial and military aircraft have continued to raise concern about acoustic radiation from jets. This has motivated new research on noise production and propagation mechanisms in both perfectly and imperfectly expanded conditions. Several review articles provide overview snapshots of the state-of-the-art [1–5]. Major recent advances have leveraged the better understanding to derive low rank models of turbulent fluctuations [6–9] and relatively simple tools for noise predictions [2, 10–13]. These efforts are interrelated since the growth and decay of large scale turbulent structures, which are the dominant dynamic feature of jet turbulence, have also been linked to the peak turbulent mixing noise emitted in the downstream shallow angle direction [1].

Most studies in this vein have addressed jets issuing from circular nozzles, which display inherent symmetries that can be exploited for model simplification. A cylindrical coordinate system is a natural choice for these jets and it simplifies the application of the azimuthal periodicity property of the statistics through an azimuthal Fourier series decomposition, offering several advantages. For example, Michalke and Fuchs [14] showed that the fluctuating pressure field of a turbulent circular jet could be represented to reasonable accuracy with only the first three azimuthal modes, since they contain most of the fluctuation energy, allowing for significant data reduction by a truncation of the Fourier series beyond the leading terms. Moreover, Schmidt *et al.* [7] used Spectral Proper Orthogonal Decomposition (SPOD) to show that the axisymmetric and first azimuthal mode exhibit pronounced low-rank behavior for

---

[*] chakrabarti.23@osu.edu; Mechanical and Aerospace Engineering, The Ohio State University,
Columbus, Ohio, 43210

[†] gaitonde.3@osu.edu

[‡] usasidharannair@fsu.edu

a range of acoustically significant frequencies. In addition to these advantages, an azimuthal homogeneity arising out of the polar symmetry of circular jets further simplifies their modelling [6, 15].

Besides data driven methods like Fourier analysis or Proper Orthogonal Decomposition (POD), the linear Navier-Stokes operator can also be used to model the dominant dynamic features of the jet [16]. Gudmundsson and Colonius [8] used the linear framework of the Parabolized Stability Equations (PSE) to model coherent fluctuations in the jet and demonstrated close agreement with the nearfield low frequency turbulent statistics for the first three azimuthal modes. The assumption of mean flow homogeneity in the azimuthal direction, used in several earlier linear analyses, can also be relaxed as shown by Lajús *et al.* [17] who used Floquet theory to model the axisymmetric instability waves of corrugated jets. While such studies lay the groundwork for a linear analysis of the azimuthal modes of more complex rectangular jet flowfields, the turbulence statistics of the azimuthal Fourier modes in rectangular jets have not yet been analyzed.

In addition to modeling turbulent fluctuations in the jet, the azimuthal Fourier basis is also particularly suited to the problem of jet aeroacoustics because higher azimuthal modes have lower acoustic efficiency [18], and thus have a progressively smaller impact on the peak acoustic radiation in the downstream shallow angle direction. This is also corroborated by experimental results, where the peak jet noise field is found to be predominantly axisymmetric. Cavalieri *et al.* [19] further showed that higher azimuthal Fourier modes ($m = 1$ and $m = 2$) of circular jets contribute progressively less with increasing Mach number, and have a relatively minor influence in transonic and supersonic jets.

These favorable properties of azimuthal Fourier modes, coupled with an improved understanding of jet turbulence, have led to the development of a variety of models for jet acoustic radiation. These can be broadly categorized into dynamic and kinematic models. The former educe the farfield acoustic radiation based solely on the dominant dynamical features of the jet. For instance, Sinha *et al.* [20] were able to capture the two leading azimuthal modes of the farfield acoustics of a circular supersonic jet with appreciable accuracy using both a PSE framework established by Gudmundsson and Colonius [8], as well as the leading SPOD modes of the jet. Kinematic models, on the other hand, employ carefully chosen statistics within the core of the jet, with some empiricism, to model the acoustic source field and have received significant attention in recent years [2, 10, 13, 21]. Some of these kinematic models have shown that the statistics of the fully turbulent flow can yield erroneous farfield acoustics [22]. Given the acoustic significance of the axisymmetric azimuthal mode, better results are obtained when quantities such as the amplitude envelope [11], two point coherence length [22], and cross spectral density are evaluated for the axisymmetric azimuthal mode alone instead of the full turbulent data. Thus, azimuthal mode decomposition of fluctuation data is a key component of most acoustic models for circular jets.

While much of the literature cited above has focused on circular jets, interest in rectangular jets has grown in recent years. Among their advantages are higher rates of entrainment [23, 24], thrust vectoring potential, and easier airframe integration. The nearfield dynamics of rectangular jets, however, are more complex than those of circular jets, and can include axis-switching [25, 26], preferential flapping in the minor axis direction [27, 28], warping of azimuthal vortex rings [29, 30], and different forms of streamwise vorticity generation [26]. These features can manifest their signature in the farfield acoustics as well. In addition to the variables that affect the dynamics and acoustics of circular jets such as operating conditions, rectangular jets are characterized by their aspect ratio [31] and upstream duct geometry [26].

Bridges [31] performed a detailed comparison of the acoustics of circular and rectangular jets. Key findings were that the farfield acoustics of low $AR$ rectangular jets were essentially axisymmetric and closely matched those of a similarly sized circular jet. However, at high $AR$ such as $AR = 8$, several distinct features emerged relative to circular jets. While qualitative features such as superdirectivity were retained, the minor axis direction exhibited 2 dB excess farfield acoustic radiation compared to the major axis direction, marking a loss in the acoustic axisymmetry.

The rectangular jet aeroacoustic field is also affected by imperfect expansion in a manner distinct from circular jets. For example, Veltin and McLaughlin [32] found the minor axis plane of an $AR = 1.75$ jet to be 3 dB louder than the major axis plane in the sideline direction due to the shock component of the noise. This disparity, however, did not significantly affect the peak noise in the downstream shallow angle direction which remained axisymmetric for this AR. Heeb *et al.* [33] also measured noise in the downstream shallow angle direction to be axisymmetric for an AR=2 shock-containing jet. Thus, although there are a variety of flowfield differences, the peak noise from low AR jets in the downstream shallow angle direction is similar to that of circular jets for a range of operating conditions [34].

Despite qualitative similarities such as superdirectivity and acoustic axisymmetry (for low $AR$), many of the sophisticated analyses tools developed for the circular jet acoustics have not been extended to rectangular jets. One of the difficulties encountered is that unlike the azimuthal Fourier modes for circular jets, there is no obvious set of spatial functions in which to expand the instantaneous statistics of rectangular jets. Kinzie and McLaughlin [35] address the related problem for elliptical jets by considering Mathieu functions, which have an elliptical variation in the azimuthal direction, in line with the shape of the nozzle exit. The sharp corners of rectangular jets pose an even greater difficulty in the isolation of such functions. Additionally, the form of the plume can change quite drastically downstream of the nozzle exit due to axis-switching, rendering spatial functions derived for a specific nozzle exit shape less useful in these regions. Even if such functions are found, they may not possess the many simplifying characteristics of Fourier modes, such as mutual orthogonality and decreasing acoustic efficiency.

Techniques to deploy an azimuthal Fourier decomposition for rectangular jets have the potential to vastly simplify their analyses and facilitate adaptation of key modeling procedures from those evolved for circular jets. The utility of any azimuthal mode decomposition for rectangular jets can be broken down into a test for two features. First, a rapid convergence of the instantaneous statistics of the jet in the azimuthal Fourier space is desired, since this fosters a simplified error bound truncation of the Fourier series beyond the dominant modes. Unlike for circular jets, this property is not guaranteed for rectangular jets since a projection on a cylindrical coordinate system, necessary for the azimuthal Fourier decomposition, may not be well suited due to a lack of polar symmetry. This is especially true for the region near the nozzle exit where such jets are predominantly rectangular in cross section; sharp corners immediately downstream of the nozzle exit may require infinitely many Fourier modes for a complete representation. Nonetheless, instabilities arising at the corners of rectangular jets in the near nozzle region smooth out mean flow gradients [36], which may help ameliorate this difficulty. Recently, Chakrabarti *et al.* [37] demonstrated promising preliminary results in reconstructing the instantaneous statistics of an $AR = 4$ rectangular jet using the leading azimuthal modes.

The second, related, desired feature is an ability to reconstruct the Overall Sound Pressure Levels (OASPL) using the leading Fourier modes. In circular jets, azimuthal homogeneity of the statistics enables a reconstruction of the RMS of fluctuations as the sum of squares of the RMS of individual modes; this greatly reduces the complexity of modeling [15, 19]. The lack of azimuthal statistical homogeneity in rectangular jets introduces additional complication, since it implies that constructive interference between all pairs of azimuthal modes must be accounted for while reconstructing the RMS. However, some simplification is afforded by leveraging mirror symmetry of rectangular jets along the minor and major axis planes. Verifying the applicability of such simplifying techniques for rectangular jets is thus non-trivial.

The present work thus examines ways of using azimuthal decomposition approaches to facilitate the description of rectangular jet evolution for a range of aspect ratios. Specifically, we examine the statistics of the leading azimuthal modes of rectangular jets and assess their features relative to those of a circular jet. To that end, Large-Eddy Simulations (LES) are performed for rectangular jets of $AR$s 1, 4, and 8 along with a circular jet of equivalent diameter. The details of the numerical algorithm and flow conditions used, are described in section II. Key differences between the rectangular and circular jets, including critical mean flow parameters and the farfield acoustics, are highlighted in section III. Although the pressure field is typically employed for such procedures, we rely primarily on an acoustic variable derived from a physics-based fluid thermodynamic (FT) component (vortical, acoustic, and entropic) decomposition of the turbulent fluctuation field [38]. The FT decomposition provides greater insights into the acoustic dynamics and improves the convergence of modal decomposition techniques [39]; a summary of this decomposition and dominant features of the individual FT components of the rectangular jets are presented in section IV. The effectiveness of azimuthal decomposition is investigated by mapping fluctuation fields onto a cylindrical mesh. The consequences of the departure from axisymmetry are then evaluated in section V by examining the dynamics of higher azimuthal Fourier modes of the acoustic fluctuations. The implications of the azimuthal inhomogeneity of rectangular jets as well as some specific dynamic features associated with their nearfield asymmetry are discussed in section VI. Using these considerations, a reduced order model for rectangular jets is developed in section VII using only three leading azimuthal modes. Finally, a summary of the paper is presented in section VIII.

## II. METHODOLOGY

The non-dimensionalized compressible Navier-Stokes equations cast in the strong conservation form are solved in a curvilinear coordinate $(\xi, \eta, \zeta)$ frame with $J$ being the Jacobian of the curvilinear transformation given by $\left(J = \frac{\partial(\xi,\eta,\zeta,\tau)}{\partial(x,y,z,t)}\right)$ [40].

$$\frac{\partial}{\partial \tau}\left(\frac{\overrightarrow{q}}{J}\right) + \frac{\partial \hat{F}}{\partial \xi} + \frac{\partial \hat{G}}{\partial \eta} + \frac{\partial \hat{H}}{\partial \zeta} = \frac{1}{Re}\left[\frac{\partial \hat{F}_\nu}{\partial \xi} + \frac{\partial \hat{G}_\nu}{\partial \eta} + \frac{\partial \hat{H}_\nu}{\partial \zeta}\right] \tag{1}$$

where $\overrightarrow{q}$ refers to a vector comprised of the conserved variables. Thus, $\overrightarrow{q} = [\rho, \rho u, \rho v, \rho w, \rho E]^T$. The vectors $\hat{F}$, $\hat{G}$ and $\hat{H}$ correspond to the inviscid fluxes and the vectors $\hat{F_\nu}, \hat{G_\nu}, \hat{H_\nu}$ constitute the viscous fluxes. For example,

$$F = \begin{bmatrix} \rho\hat{U} \\ \rho u\hat{U} + \xi_x p \\ \rho v\hat{U} + \xi_y p \\ \rho w\hat{U} + \xi_z p \\ (\rho E + p)\hat{U} \end{bmatrix} \quad and \quad F_\nu = \begin{bmatrix} 0 \\ \xi_{x_i}\sigma_{i1} \\ \xi_{x_i}\sigma_{i1} \\ \xi_{x_i}\sigma_{i1} \\ \xi_{x_i}(u_j\sigma_{ij} - \Theta_i) \end{bmatrix} \tag{2}$$

The contravariant velocity component is given by $\hat{U} = \xi_x u + \xi_y v + \xi_z w$ and the specific energy density is

$$E = \frac{T}{\gamma(\gamma-1)M_j^2} + \frac{1}{2}(u^2 + v^2 + w^2) \tag{3}$$

The deviatoric stress ($\sigma_{ij}$) and heat flux vector ($\Theta_i$) are given by:

$$\sigma_{ij} = \mu\left(\frac{\partial\xi_k}{\partial x_j}\frac{\partial u_i}{\partial\xi_k} + \frac{\partial\xi_k}{\partial x_i}\frac{\partial u_j}{\partial\xi_k} - \frac{2}{3}\frac{\partial\xi_l}{\partial x_k}\frac{\partial u_k}{\partial\xi_l}\delta_{ij}\right) \tag{4}$$

$$\Theta_i = -\frac{1}{(\gamma-1)M_j^2}\left(\frac{\mu}{Pr}\right)\frac{\partial\xi_j}{\partial x_i}\frac{\partial T}{\partial\xi_j} \tag{5}$$

Stokes' hypothesis is assumed for the bulk viscosity coefficient *i.e* $\lambda = -2/3\mu$. Further details of the derivations may be found in Vinokur [41]. Flow velocities and density are normalized by the jet exit velocity ($u_j$) and density ($\rho_j$), respectively while the pressure is non-dimensionalized by $\rho_j U_j^2$; the perfect gas relationship then reads ($p = \rho T/\gamma M_j^2$), where $M_j$ refers to the jet exit Mach number. A constant Prandtl number of 0.72 is assumed along with a constant ratio for the specific heats ($\gamma = 1.4$). Sutherland's law is used to model the temperature dependence of viscosity.

To ensure consistency with the literature for circular jets, and an even basis of comparison, the length-scale is chosen as the diameter of a circular nozzle with an equal exit area as the rectangular nozzles being studied (equivalent diameter $D_e$). The non-dimensional length of the major axis ($l$) as a function of the $AR$ is given by:

$$\frac{l}{D_e} = \sqrt{\frac{\pi(AR)}{4}} \tag{6}$$

For reference, fig. 1a. shows the nozzle exit cross sections of the jets being studied. In order to preserve a constant exit area, the minor axis length of the nozzle progressively decreases with increasing $AR$, the impact of which is assessed with the results.

The flow parameters are chosen to be representative of conditions examined in the literature. For concreteness, perfectly expanded conditions are chosen at a design Mach number of 1.3 and a Reynolds number $10^6$, patterned after extensive experimental [42–44] and numerical studies [45–48]. Furthermore, the goal of evaluating distinctions between the different $AR$ and the circular nozzles necessitates similar nozzle exit conditions for all cases, since these can affect the downstream growth of the plume [49–51]. For this reason, a uniform laminar nozzle exit velocity profile is chosen for all cases, similar to those of Gaitonde [45], Gaitonde and Samimy [46]. This approach has previously provided good agreement with the circular jet data of Samimy *et al.* [42]. Additionally, lower inflow turbulence levels enhance phenomena specific to rectangular jets, such as axis-switching [23, 49], and thus provide a suitable testbed for the azimuthal Fourier analysis. The farfield and downstream boundaries are at 10 $D_e$ and 40 $D_e$ from the nozzle exit respectively. The mesh is gradually stretched out starting at $5D_e$ from the individual shear layers in the cross stream direction and 35 $D_e$ from the nozzle exit in the streamwise direction to provide a suitable sponge condition. A method of characteristics boundary condition is used on the outflow boundary ([52]).

The Roe scheme is used for the inviscid fluxes [53] with a third-order reconstruction using the MUSCL approach [54]. Viscous terms are discretized with a second order central differencing technique. Following Pulliam and Chaussee [55], the temporal integration is performed using an approximately factored second order Beam Warming scheme with two sub-iterations. The rectangular jets are simulated using stretched Cartesian meshes, shown for example for the $AR$ = 4 jet in fig. 1b-d. The circular reference jet mesh has been presented in the literature [46]. The streamwise ($\Delta x = 0.023D_e$ at the nozzle exit) and cross-streamwise mesh spacing ($\Delta y = 0.005D_e$ along the lipline) are chosen based on numerous prior studies using the same solution procedure at similar Mach (1.3) and Reynolds ($10^6$) numbers. The meshes employed for the rectangular jets comprise $15 \times 10^6$ points while that for the circular

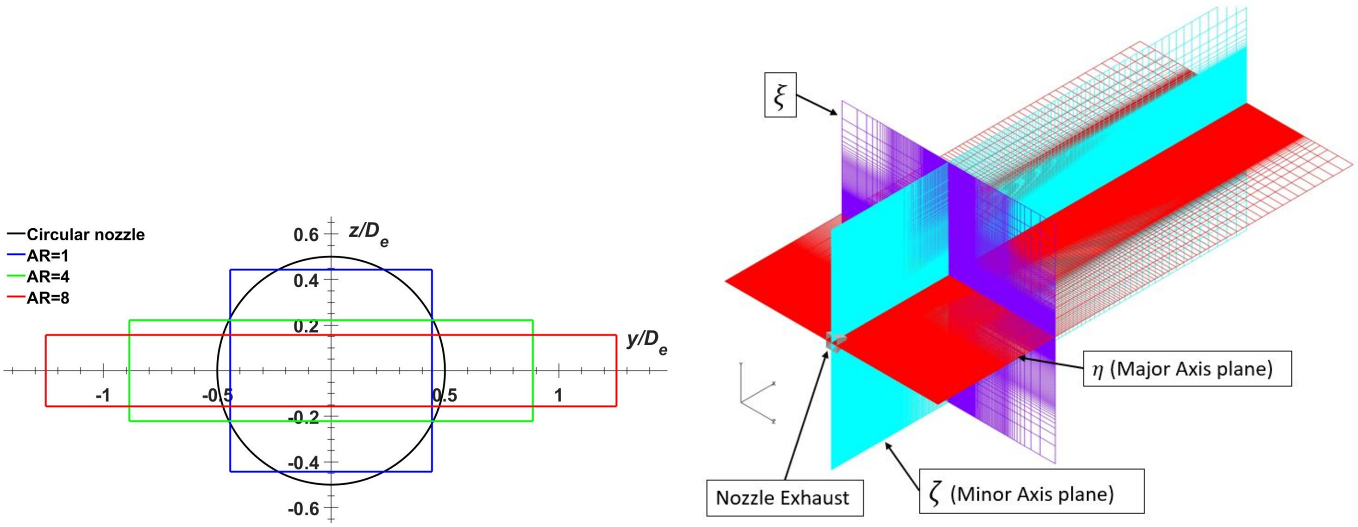

(a) Nozzle exit profiles (b) Mesh structure

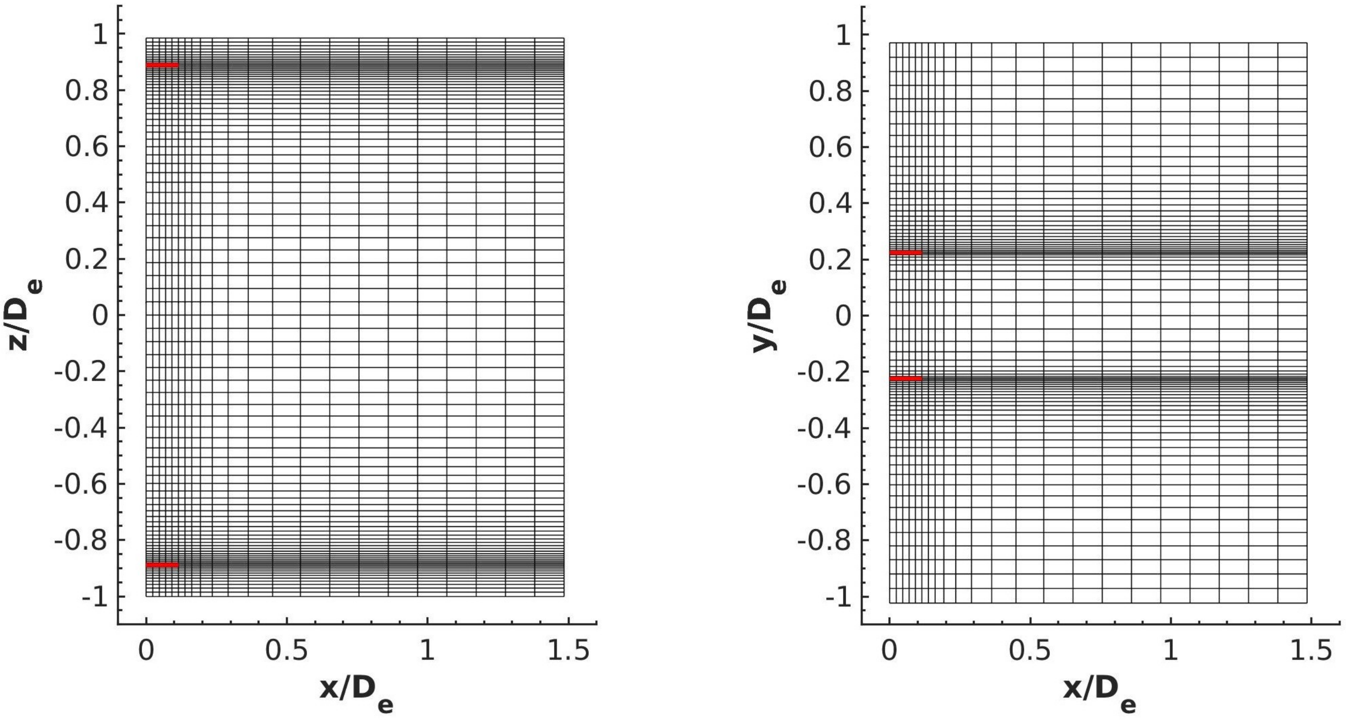

(c) Major axis grid (nozzle sleeve in red) (d) Minor axis grid (nozzle sleeve in red)

FIG. 1: Characteristics of inflow and spatial discretization

jet uses $18 \times 10^6$. Note that the internal structure of the nozzle, such as considered in Chakrabarti *et al.* [56], is not simulated since differences between plume development cannot then be ascribed solely to the nozzle exit profiles of interest. Prior mesh-converged results using similar grid sizes have successfully reproduced experimental measurements of mean centerline velocity fields, near-acoustic field, turbulent kinetic energy, and shallow-angle and farfield noise for both circular [45, 48] and rectangular jets [56].

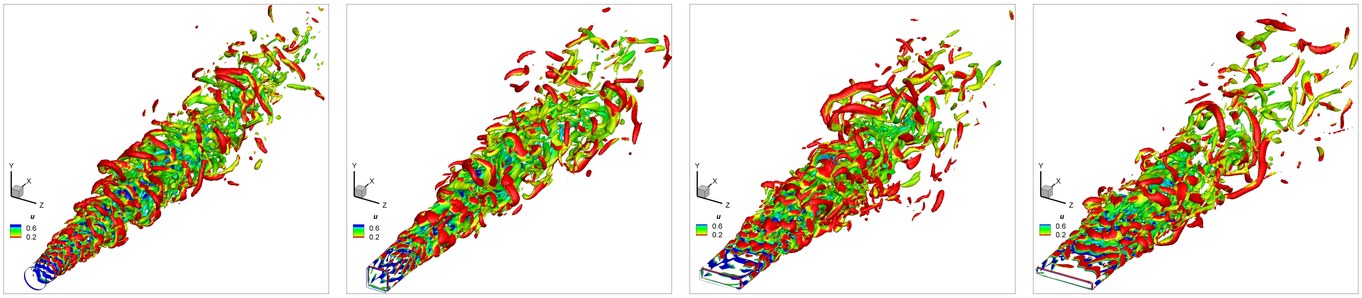

(a) Circular jet (b) $AR = 1$ (c) $AR = 4$ (d) $AR = 8$

FIG. 2: Iso-surfaces of Q-criterion (Q=1) colored by streamwise velocity

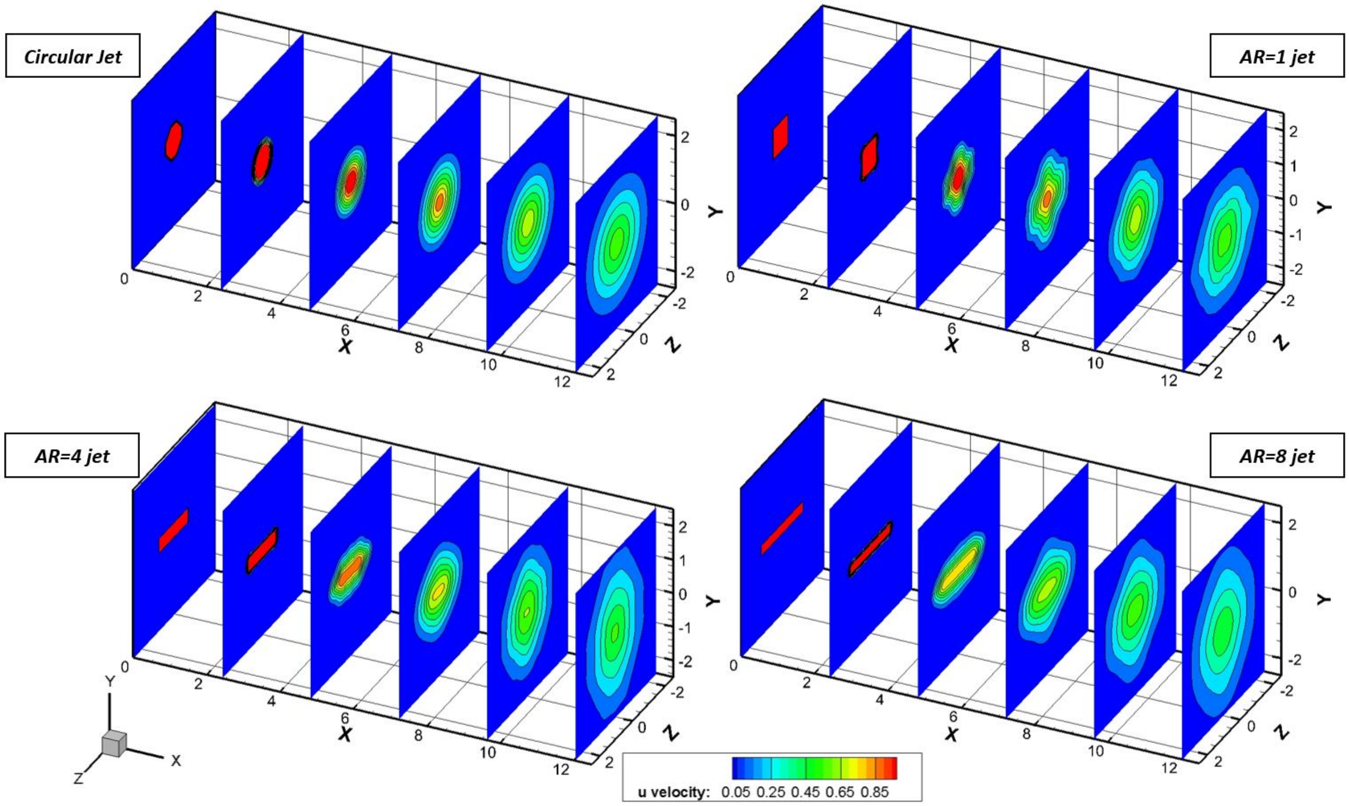

FIG. 3: Contours of mean streamwise velocity at several axial stations showing the spatial development of the jets

## III. OVERALL FLOWFIELD FEATURES

Figure 2 shows instantaneous snapshots of each simulated flowfield using iso-surfaces of Q-criterion ($Q = 1$) colored by the streamwise velocity component. The wide spectrum of scales resolved by the LES can be clearly discerned. The figures also show increased jet spreading rate with $AR$, similar to the observations of Grinstein [23], Gutmark and Grinstein [24], who linked this behaviour to higher entrainment than in circular jets; this also results in large scale structures spreading further from the axis in higher $AR$ jets.

The mean flow field facilitates a more systematic assessment of the spatial development with implications to the unsteady dynamics. For instance, in circular jets, the potential core length is correlated with the length-scale across which coherent structures grow and decay prior to turbulent breakdown and is significant for jet aeroacoustic modeling [11]. Figure 3 shows contours of mean streamwise velocity at several axial stations for each jet. The square jet ($AR = 1$) cross section undergoes a $45^o$ rotation downstream of the nozzle exit, so that the diagonals are reoriented along the initially flat sides of the jet; this is most clearly evident at $x = 5D_e$. Similar phenomena observed

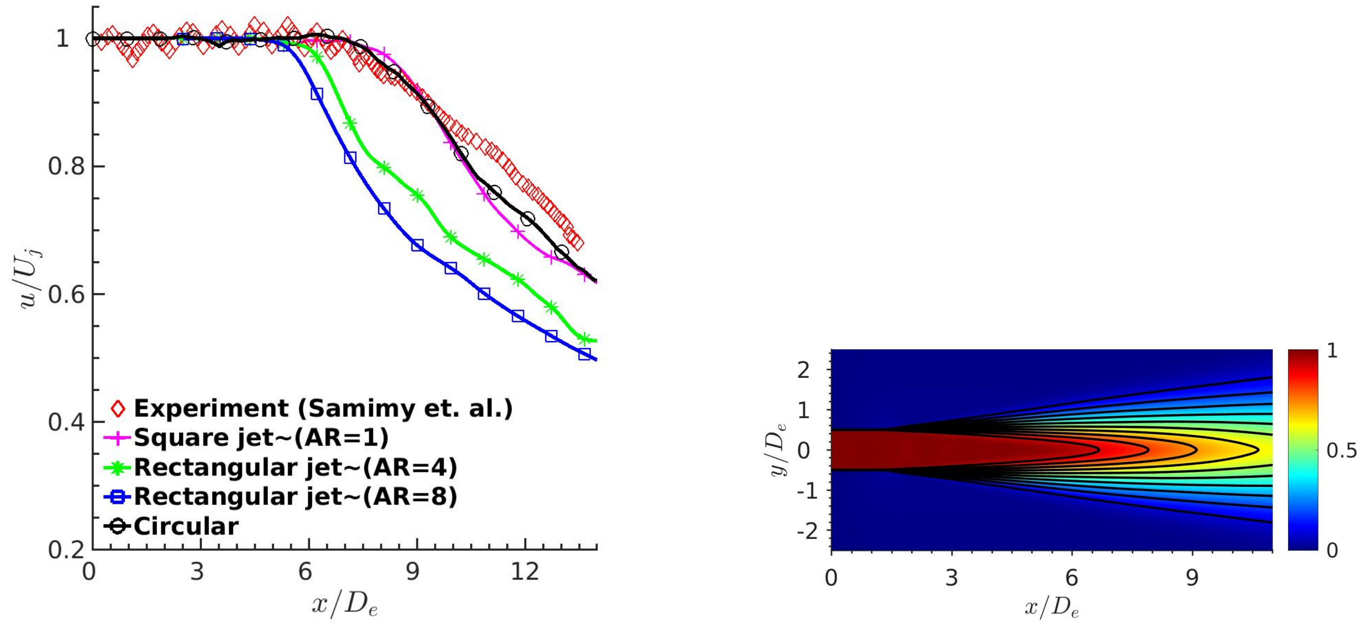

(a) Centerline

(b) Circular jet

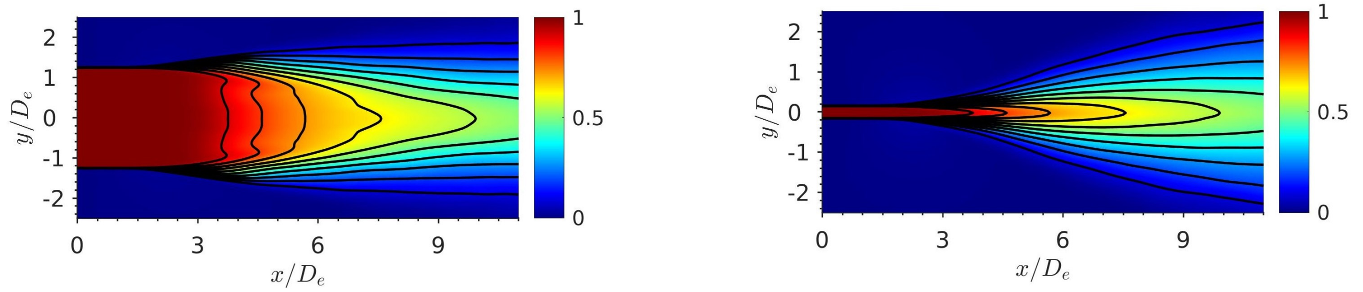

(c) $AR = 8$ major axis plane

(d) $AR = 8$ minor axis plane

FIG. 4: Effect of the $AR$ on the length of the potential core shown using streamwise mean velocity

in triangular jets have been associated with corners in nozzle shapes [24]. For square jets, the effect is more pronounced for lower inflow turbulence levels [57]. By $x = 10D_e$, however, the square jet ($AR = 1$) displays an axisymmetric cross-section and is not very different from the circular jet at the same axial station. The jets from the higher $AR$ nozzles however, develop differently, since they combine the effects of the corners in the nozzle geometry with the influence of unequal characteristic lengths as in elliptic jets [29]. Crucially, these jets do not evolve to an axisymmetric form. Axis-switching is evident in the $AR = 4$ and $AR = 8$ jets, resulting in a predominantly elliptical mean flow cross-section that is wider along the minor axis plane by $x/D_e = 10$ and $x/D_e = 12$ respectively. Axis-switching of high $AR$ rectangular and elliptic jets is also more pronounced for low nozzle exit turbulence levels as noted in the previous section.

The collapse of the potential core is examined using the mean streamwise velocity. Values along the jet centerline are shown in fig. 4a. along with the experimental data of Samimy *et al.* [42] for the circular jet; the undulations in mean streamwise velocity near the nozzle exit are caused by a weak shock train in the core of the jet and result from a slight mismatch between the reservoir and ambient conditions [43]. Similar to previously reported computational studies where the inflow conditions are not known [46, 47, 58], the experimental core length is employed as a reference to highlight the decay rate downstream of the potential core collapse. The potential core length of the rectangular jets is smaller than that of the circular jet, and decreases with $AR$. This is most evident for the $AR = 8$ jet whose potential core length (based on 90% of the jet exit velocity) is about $3D_e$ shorter than the circular jet. The reason is evident from the cross sectional plane data of fig. 4: increasing $AR$ while maintaining the nozzle exit area results in a shortening of the minor axis length (fig. 1a) and thus the distance between the shear layers on the longer nozzle sides. These growing shear layers converge at relatively shorter streamwise distances from the nozzle exit. This effect was investigated by Chakrabarti *et al.* [56] in the context of an $AR = 2$ rectangular jet and by Chakrabarti *et al.* [37] for an $AR = 4$ jet. These results are consistent with those of Krothapalli *et al.* [59], who modeled the decay of the mean centerline streamwise velocity of a low speed, high $AR$ jet, with power laws for three distinct regions. For such jets, shear layers on the minor axis plane converge to the centerline within a shorter streamwise distance compared to those on the major axis plane, resulting in a streamwise velocity decay that follows the same power law as a planar jet. The axisymmetric power law for streamwise velocity decay was recovered further downstream. While the present, much higher velocity, rectangular jets do not exhibit these distinct decay regions, the convergence effects of the shear layers on the minor axis plane towards the centerline is similar and manifests as a decrease in the potential core length.

For subsequent reference, the OASPLs are examined to delineate the effect of the $AR$ on acoustic intensity and directivity. The Ffowcs-Williams and Hawkings (FWH) analogy [60] is used in the frequency domain as in Mendez *et al.* [61]. Data over 100 characteristic times (defined based on the jet exit velocity and nozzle equivalent diameter) were interpolated on a cylindrical surface three equivalent diameters away from the axis of each jet. The FWH surface extends to the downstream end of the domain, where eddies are dissipated out using sponge zones, precluding the need for end caps discussed by Mendez *et al.* [61]. The farfield acoustic spectra (Sound Pressure Levels (SPL)) are obtained at several geometric points around the jet and the OASPL is then obtained by integrating across the frequency band of interest ($St_{D_e}\epsilon[0.1, 1]$). A validation exercise for this procedure may be found in Chakrabarti *et al.* [37]

The azimuthal and polar angles with respect to the nozzle exit are shown schematically in fig. 5a. Figure 5b through d display the variation of the OASPL with polar angle ($\theta$) at various azimuthal angles ($\phi$) for each jet simulated. The square jet (fig. 5b) is acoustically similar to the circular jet, as evidenced by its axisymmetric noise intensity and close correspondence with the peak radiation intensity and direction of the latter. With increasing $AR$, however, two key trends become apparent. First, the axisymmetry of the farfield acoustic radiation is distorted; for the $AR = 8$ jet, a 2 dB variation in noise intensity is observed around the azimuth (fig. 5d). The minor axis plane of this jet is louder than the major axis plane, matching the observations of several previous studies on rectangular jets [31, 62]. Second, with increasing $AR$, the peak acoustic radiation decreases slightly and its direction moves progressively to lower polar angles (towards the sideline direction), similar to the results of Bridges [31].

## IV. FLUCTUATION FIELDS EXAMINED

The most common variable used for azimuthal mode decomposition of circular jets is typically the pressure fluctuation, $p'$ [7, 11, 14, 20, 63]. In regions far from the turbulent fluctuations, the relationship of $p'$ to the acoustics is direct. In the near-acoustic field, however, $p'$ is characterized by both acoustic and hydrodynamic content [64, 65]. A direct observable consequence is the scale disparity between the pressure fluctuations in the near versus farfields of jets [10]. This property of $p'$ can affect conclusions on the convergence of azimuthal modes, and motivates approaches to isolate an acoustic component for analysis. $p'$ splittings have been derived through several data driven techniques [65–67]. An alternative definition of an acoustic field, that avoids user-defined criteria, has recently been obtained through the physics-based decomposition provided by momentum potential theory [38]. The approach, summarized below, splits the turbulent field into FT components, *i.e.*, hydrodynamic, acoustic, and thermal fluctuations. Application to LES of circular jet flows [48] reveal several attractive properties. The acoustic component displays a jittering, spatio-temporally modulated wavepacket form with radial decay rate, farfield Power Spectral Density (PSD) and phase speeds that are consistent with those expected from the literature. More pertinent to this work, the acoustic component also yields better convergence of parameters for kinematic farfield noise models, than $p'$ [39]. In order to extract the FT components, a Helmholtz decomposition of the "momentum-density" field ($\rho\mathbf{u}$) is used to define (vector) acoustic (irrotational and isentropic fluctuations, $-\nabla\psi'_A$), thermal (irrotational and isobaric fluctuations, $-\nabla\psi'_T$)) and vortical/hydrodynamic solenoidal fluctuations ($\mathbf{B}'$) components. The vector fields satisfy the following governing equations [38]:

$$\nabla^2\psi'_A = -\frac{1}{c^2}\frac{\partial p'}{\partial t} \tag{7}$$

$$\nabla^2\psi' = -\frac{\partial \rho'}{\partial t} \tag{8}$$

$$\mathbf{B}' = \rho\mathbf{u} - \overline{\rho\mathbf{u}} - \nabla\psi' \tag{9}$$

$$\psi'_T = \psi' - \psi'_A \tag{10}$$

The spatio-temporally resolved fluctuation fields from the LES are used as the source fields of the Poisson equations 7 and 8 to obtain the acoustic potential ($\psi'_A$) as well as the total irrotational potential ($\psi'$). The latter, along with the LES data for the "momentum-density" field ($\rho\mathbf{u}$), is then used to evaluate the hydrodynamic fluctuations

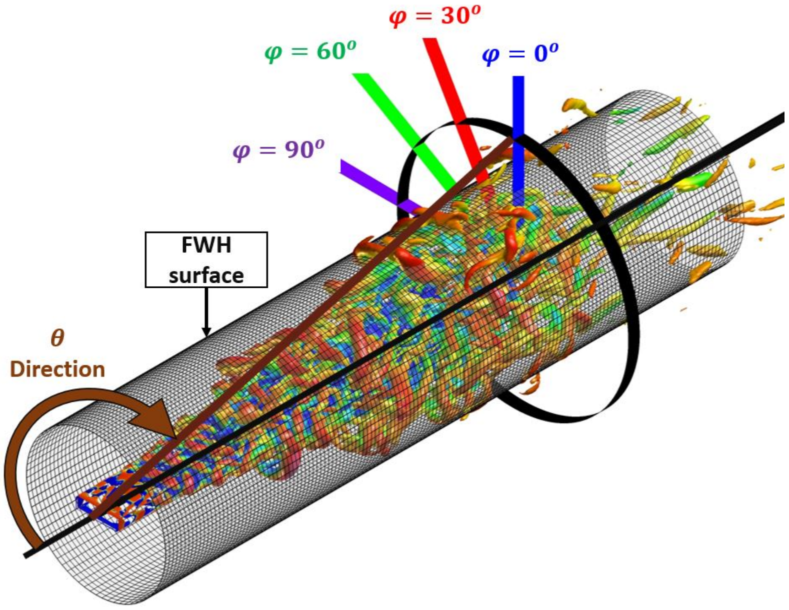

(a) Schematic of azimuthal ($\phi$) and polar ($\theta$) angles along with the FWH surface

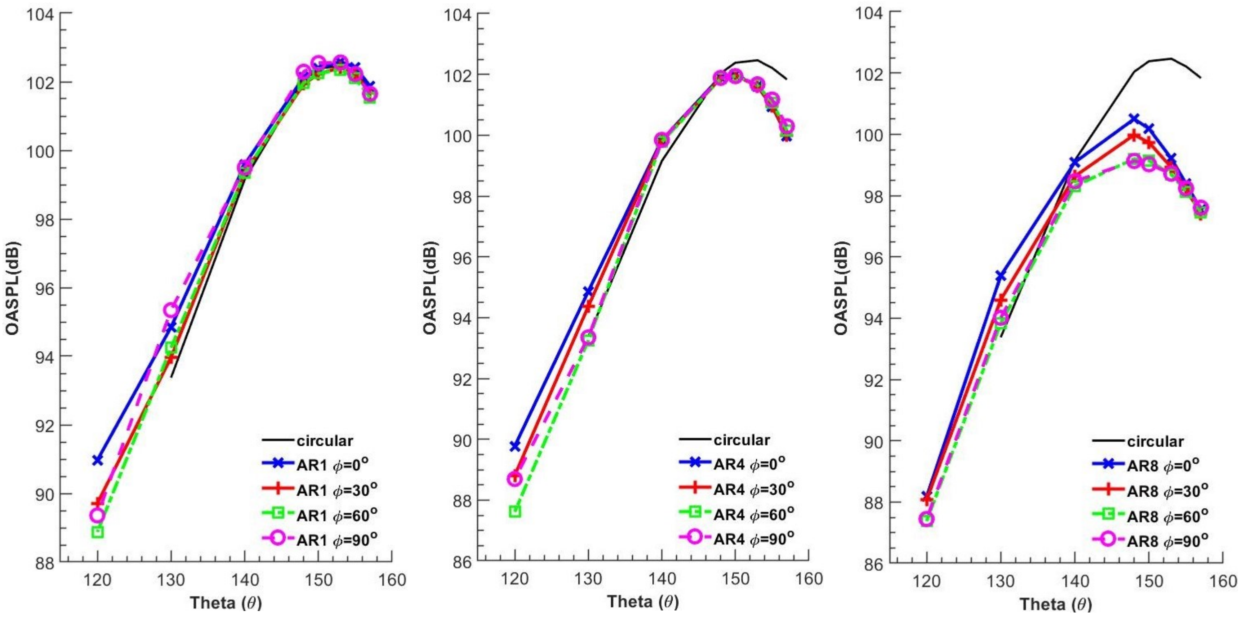

(b) $AR = 1$ (c) $AR = 4$ (d) $AR = 8$

FIG. 5: Variation of farfield OASPL (Over All Sound Pressure Level) with polar angle for jets of various $AR$

per equation 9. Finally, the thermal fluctuation potential ($\psi'_T$) is obtained using equation 10. Algorithmic details and additional properties of the decomposition may be found in [48, 68].

Figure 6 shows instantaneous iso-surfaces of the the acoustic, hydrodynamic, and pressure fluctuations for each case. Here and below, the streamwise components of acoustic and hydrodynamic fluctuations ($\frac{\partial \psi'_A}{\partial x}$ and $B'_x$) are plotted; these are the largest components, and facilitate better contrast because of their positive and negative values. For simplicity, $\frac{\partial \psi'_A}{\partial x}$ will be referred to as the acoustic fluctuations (or component). The magnitudes of the iso-levels are chosen to elicit the main components of the jet; these confirm that even in the rectangular cross-section cases, the hydrodynamic fluctuation magnitude is much larger than the acoustic component. The circular jet results are

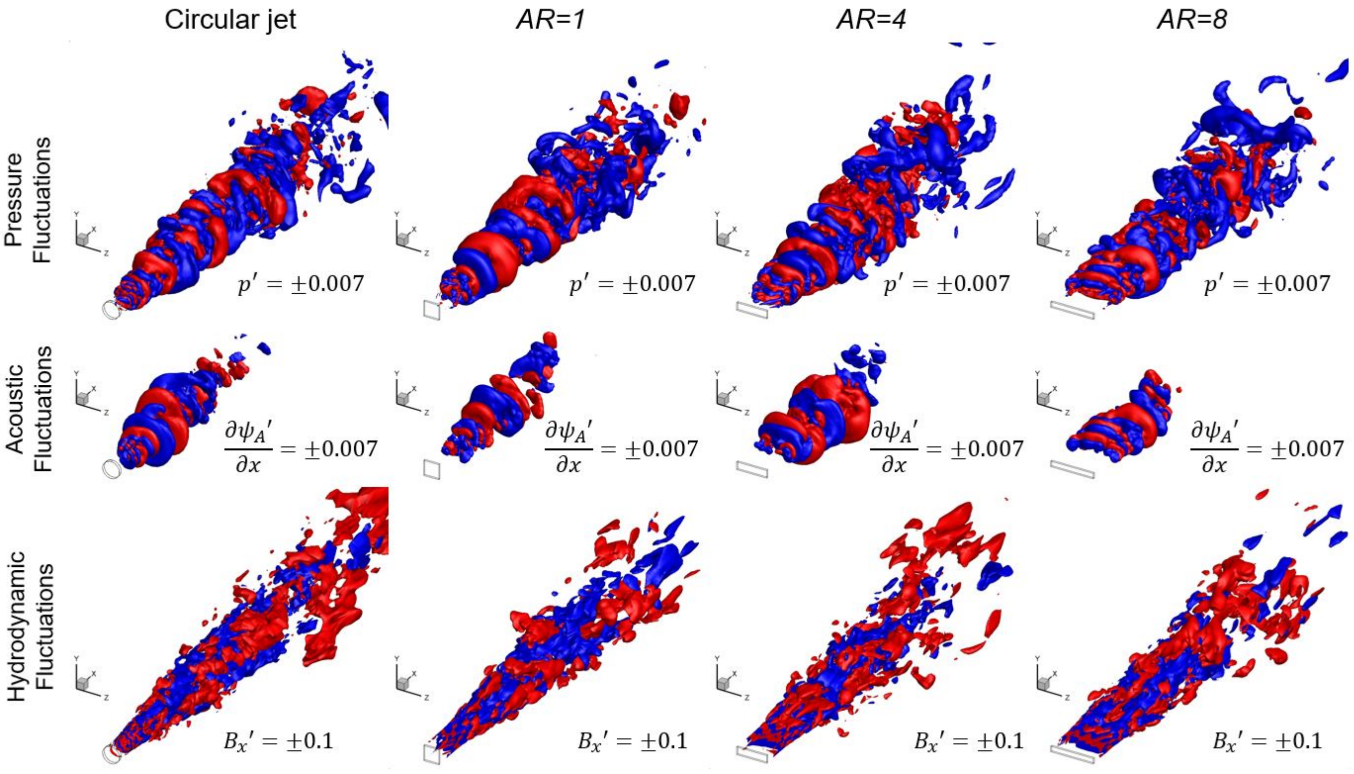

FIG. 6: Iso-surfaces of 3D snapshots of the pressure fluctuations (first row) from the LES compared with those of the acoustic (second row), and hydrodynamic fluctuations (third row) extracted from the simulated flow fields

similar to those described in the literature [39, 48]. The rectangular jets show corresponding features: hydrodynamic fluctuations are dominated by axially extended structures, reflective of a broad spatial wavenumber range and chaotic underlying jet turbulence, while acoustic fluctuations exhibit a more organized wavepacket structure with greater coherence and a compact radial support. Indeed, the acoustic fluctuations for all cases resemble a spatially modulated wavepacket with an envelope marking the growth, saturation, and decay of the waves downstream of the nozzle exit. The differences in spreading characteristics with change in $AR$ are captured primarily by hydrodynamic fluctuations.

The pressure field shows elements of both hydrodynamic and acoustic components. The initial region has the nature of a spatially growing wavepacket, similar to the acoustic fluctuating field. However, further downstream, the disorganized structure more closely resembles the hydrodynamic component. A key distinction between the acoustic fluctuations ($\frac{\partial \psi'_A}{\partial x}$) and $p'$ is thus that the former diminish rapidly beyond the potential core, whereas the latter continue to grow. This has significant implications in statistical convergence of the azimuthal decomposition properties of interest, as discussed further below. In the results below, $\frac{\partial \psi'_A}{\partial x}$ will be used most frequently, though select results with $p'$ will also be put forth for reference purposes.

## V. AZIMUTHAL MODES IN RECTANGULAR JETS

The advantages of rapid convergence of fluctuation statistics for circular jets, which allows modeling with only a few modes, motivates an examination of these statistics for nearfield rectangular jet behavior.

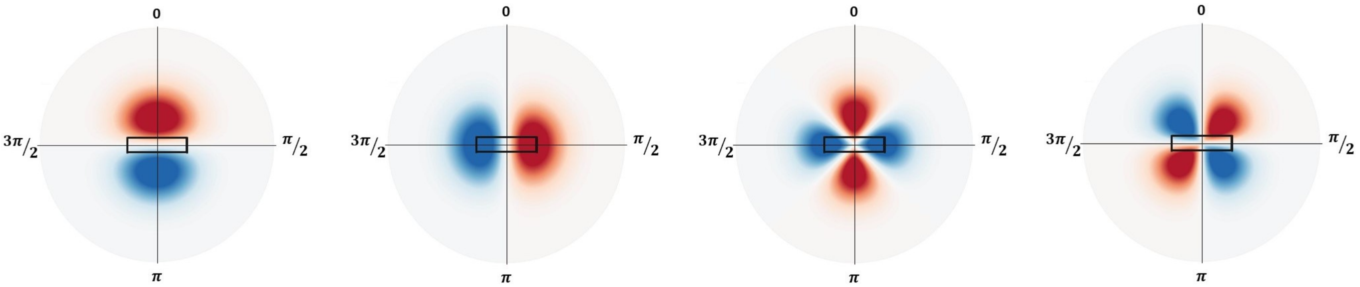

(a) mode *1a* ($\cos\phi$) (b) mode *1b* ($\sin\phi$) (c) mode *2a* ($\cos 2\phi$) (d) mode *2b* ($\sin 2\phi$)

FIG. 7: Polar plots depicting spatial distributions of the two leading azimuthally varying Fourier modes, with nozzle outline for orientation

### A. Decomposition ansatz

The Fourier decomposition is introduced in the azimuthal direction ($\phi$) in a different manner than for circular jets. Specifically, rather than the more commonly used complex exponential form [14, 18, 19],

$$q(x,r,\phi,t) = \sum_{m=-\infty}^{\infty} \hat{q}_m(x,r,t)e^{im\phi} \tag{11}$$

the following closely related ansatz provides a more convenient representation and interpretation of non-axisymmetric mechanisms:

$$q(x,r,\phi,t) = q_a^0(x,r,t) + \sum_{m=1}^{\infty} q_a^m(x,r,t)cos(m\phi) + q_b^m(x,r,t)sin(m\phi) \tag{12}$$

where, $q_a^m(x,r,t)$ and $q_b^m(x,r,t)$ refer to the 2D spatio-temporal cosine and sine Fourier coefficients respectively and $m$ refers to the azimuthal mode number, and:

$$q_a^0 = \frac{1}{2\pi}\int_{-\pi}^{\pi} q(x,r,\phi,t)d\phi; \qquad q_a^m = \frac{1}{\pi}\int_{-\pi}^{\pi} q(x,r,\phi,t)\cos(m\phi)d\phi; \qquad q_b^m = \frac{1}{\pi}\int_{-\pi}^{\pi} q(x,r,\phi,t)\sin(m\phi)d\phi \tag{13}$$

The relationship between the coefficients of Eq. 11 and 12 is

$$\hat{q}_m = \frac{q_a^m + iq_b^m}{2}; \qquad \hat{q}_m = \hat{q}^*_{-m} \tag{14}$$

Thus, while the complex exponential ansatz for the Fourier series uses a single complex amplitude to retain both the magnitude and phase information of the $m^{th}$ azimuthal mode, the sine-cosine ansatz of equation 12, introduces two real coefficients to retain the same information. For instance, the first azimuthal mode ($m = 1$) is given by the superposition of two waves, $q_a^1(x,r,t)\cos(\phi) + q_b^1(x,r,t)\sin(\phi)$. These will be individually referred to as $m = 1a$ and $m = 1b$, respectively, in the subsequent text. Similarly, the two waves associated with $m = 2$ will be referred to as $m = 2a$ and $m = 2b$.

The mechanisms associated with each of the above modes can be deduced from their spatial distributions, similar to the use of Mathieu functions for elliptical jets by Kinzie and McLaughlin [35]. For illustration, fig. 7 shows the components of the first and second azimuthal modes ($m = 1a, 1b$ and $m = 2a, 2b$ respectively), together with a high $AR$ nozzle exit for orientation. The mode shapes and, by extension, their individual physical interpretations necessarily depend on the choice of the azimuthal origin, $\phi = 0^o$, with respect to the major or minor axes. Choosing one of these for $\phi = 0$ greatly simplifies the analysis because of symmetry considerations, as shown below. Following Bridges [31], $\phi = 0^o$ is assigned to the minor axis plane of the nozzle exit (positive $y$-direction). Thus, mode 1a represents fluctuations that are out of phase on either side of the minor axis (fig. 7a), and are associated with flapping motion in the minor axis direction. Correspondingly, mode 1b (fig. 7b) captures flapping motion along the major axis direction. Modes $2a$ and $b$ are associated with more complex mechanisms. For elliptical jets, Kinzie and McLaughlin [35] associate mode $2a$ (fig. 7c) to “pinched” elliptical fluctuations and mode $2b$ (fig. 7d) to off-axis fluctuations.

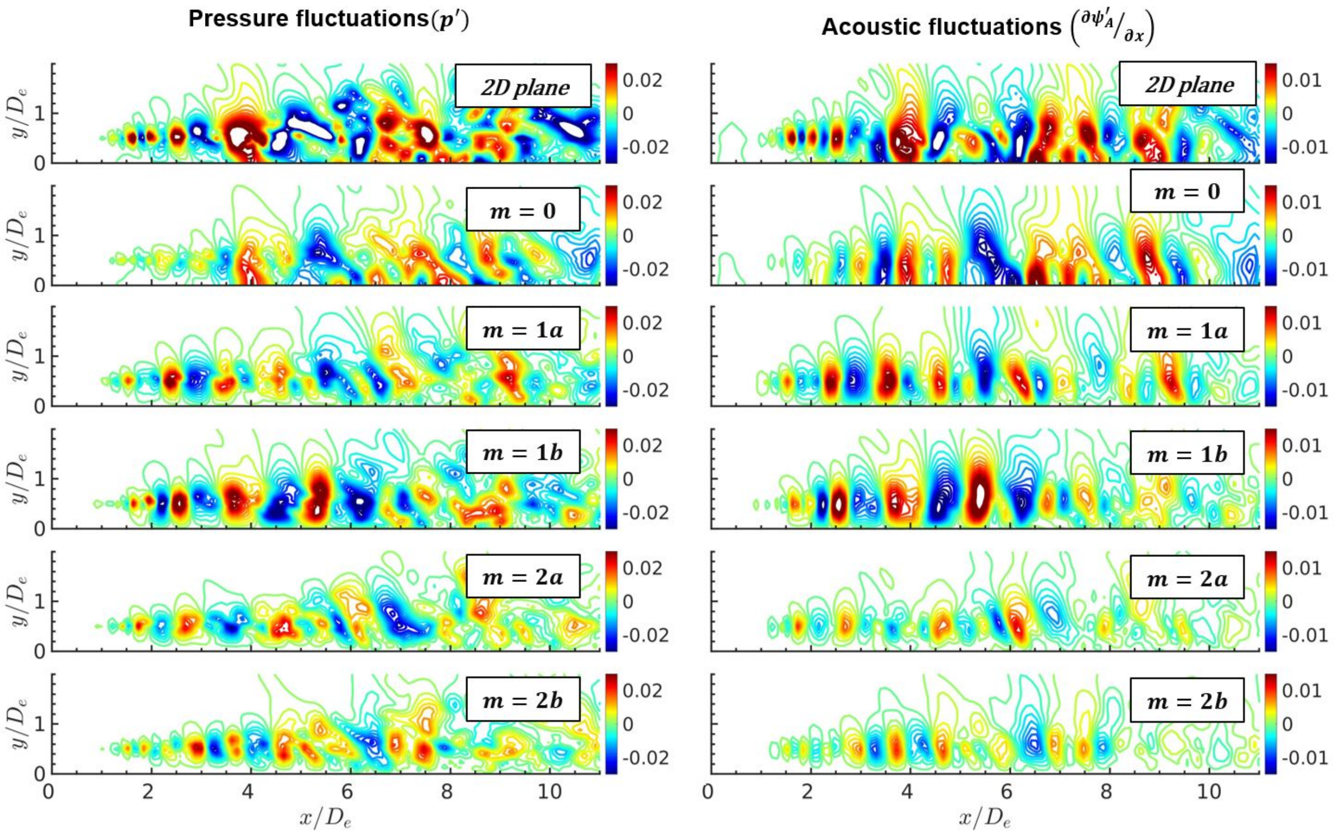

FIG. 8: Contours of pressure perturbations ($p'$, left column) and acoustic fluctuations ($\frac{\partial\psi'_A}{\partial x}$, right column) of the circular jet on a 2D cross section along with their leading azimuthal Fourier modes

### B. Rectangular modal dynamics

The well-known azimuthal modes of the circular jet [6, 14] are summarized for subsequent reference. The left column of fig. 8 shows, starting from the top, instantaneous snapshots of $p'$ on a 2D slice of the circular jet and the leading azimuthal Fourier modes, axisymmetric ($m = 0$), $1a$, $1b$, $2a$, and $2b$ respectively. A coherent wave-like structure related to the Kelvin-Helmholtz shear layer instability is apparent near the nozzle exit. Further downstream, however, the jet breaks down into finer scale turbulence. Mode $m = 0$ exhibits more coherence and filters out the finer scale turbulence downstream. The increased coherence illustrates the advantages afforded by the azimuthal mode decomposition in general, and the $m = 0$ mode in particular for round jets; its use in the construction of two-point wavepacket model parameters are discussed in Jaunet *et al.* [22]. In contrast, the finer scales in the raw pressure field, which are not as acoustically efficient, are retained in the higher azimuthal modes of the jets. No clear qualitative differences are evident between the higher azimuthal wavenumber pairs, $m = 1a$, $m = 1b$ or $m = 2a$, $2b$. The similar spatial distributions and fluctuation amplitudes of each pair is consistent with the discussion of fig. 7 and are the consequence of polar symmetry of circular jets, which is lacking in the rectangular jets examined below.

The right column of fig. 8 displays the corresponding results with the streamwise acoustic fluctuation variable ($\frac{\partial\psi'_A}{\partial x}$). Even without azimuthal decomposition, $\frac{\partial\psi'_A}{\partial x}$ displays a more organized spatial distribution and greater coherence compared to the raw pressure perturbation field; this readily highlights the advantage of this FT component over $p'$, particularly in the region downstream of the potential core collapse. The $m = 0$ mode has the form of a spatially localized wavepacket with a growth and decay envelope representing, in the aggregate, acoustic sources for downstream shallow angle noise radiation. The dominant axial length-scale of this wavepacket is a few jet diameters larger than the potential core length, beyond which the fluctuations diminish. Higher modes of the acoustic fluctuations, $1a$, $1b$, $2a$ and $2b$, also display decay in the fluctuation magnitudes, evident from the decreasing saturation of the contours in the figure. Furthermore, these higher modes also show successively sharper cutoff with streamwise distance from the nozzle exit. Both, the decreasing fluctuation magnitude and shorter streamwise lengths of the higher modes, are crucial in the acoustic source modeling of circular jets [19].

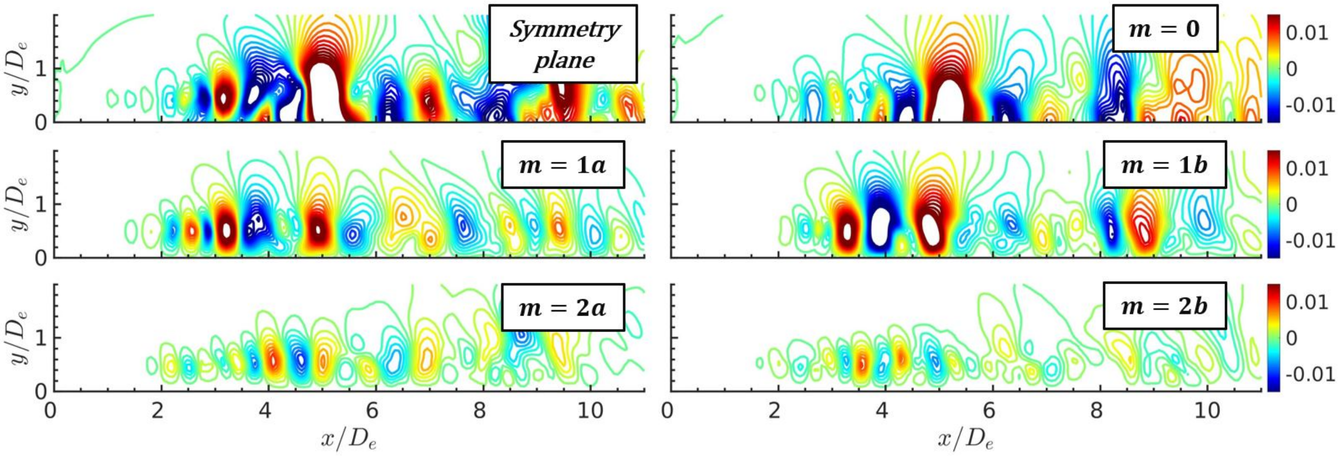

FIG. 9: The streamwise acoustic fluctuations ($\frac{\partial \psi'_A}{\partial x}$) of the $AR = 1$ jet on the symmetry plane and its leading azimuthal modes

Figure 9 shows $\frac{\partial \psi'_A}{\partial x}$ contours on the symmetry plane of the $AR = 1$ jet together with the three leading azimuthal modes (since $p'$ fluctuations are less illustrative, they are not shown). As in the case of the mean flow, the $AR = 1$ fluctuation data also show similarities with round jets, including the initial wave-like structure near the nozzle exit followed by a breakdown into more chaotic finer scale structures further downstream. Likewise, the $m = 0$ shows more coherence than the raw data, and a rapid fluctuation decay downstream of the potential core. The higher azimuthal modes exhibit progressively more rapid streamwise decay. These similarities with the circular jet are not unexpected given the rapid transformation of the square jet to an axisymmetric mean cross-section (fig. 3b).

The higher $AR$ nozzles ($AR = 4$ or $AR = 8$) however, do not transition to axisymmetric cross sections in the domain of interest as discussed in the context of fig. 3. Figure 10 shows the corresponding $\frac{\partial \psi'_A}{\partial x}$ results on the major and minor axis planes of $AR = 4$ and $AR = 8$ jet in the left and right columns, respectively. The major (black) and minor (magenta) axis liplines are also marked with dashed lines to provide a scale for reference. On the minor axis planes of both jets (fig. 10 first row), the structures associated with the initial breakdown along the lipline are similar to the circular and $AR = 1$ jets, but significantly closer to the centerline of the jet. However, on the major axis plane (second row), the fluctuation pattern is different. Two sets of structures are evident marked A and B respectively. The former sequence is closer to the centerline, with phase similar to the structures on the minor axis planes of the respective jets; these are the signatures of the lipline structures of the minor axis shear layer that essentially protrude on the symmetry plane. The outer structures, marked B, are those that evolve due to the major axis shear layers. This higher complexity is a consequence of the disparity between the distances of the major and minor axis liplines from the centerline of the jet, as the $AR$ is increased. A similar effect in the context of an $AR = 2$ jet was discussed by Chakrabarti *et al.* [56]. By an axial distance of $x = 4D_e$, however, these separate wave-trains cannot be clearly distinguished from each other.

The spatially localized wavepacket structure remains evident in the $m = 0$ modes. The shear layer structures growing along the major axis lipline (designated B earlier) do not display a discernible signature on the axisymmetric mode. Being further away from the axis, they subtend a relatively small azimuthal angle on the centerline and thus have a small contribution to the azimuthal averaging operation used to obtain the $m = 0$ mode (equation 13). Although qualitatively similar to the $m = 0$ mode in the circular and square jets, the decay with streamwise distance is more rapid, and the lobes become more radially extended. The former effect is related to the decrease in the potential core length with increasing $AR$, as discussed previously, while the latter effect is due to the effective averaging of the shear layer around the azimuth and is evaluated quantitatively in a subsequent section.

Higher azimuthal modes exhibit significant differences from their circular and square counterparts. The two components of $m = 1$, $m = 1a$ and $1b$ respectively in fig. 10, are distinct from each other, and emphasize fluctuation distributions from shear layers on the minor and major axis planes respectively. This is consistent with the directivity inherent in the two coefficients as discussed in the context of fig. 7. The chosen ansatz (equation 12) thus retains the dynamics of the two symmetry planes of the rectangular jet for $m = 1$. As a consequence, $m = 1b$ (the sine coefficient) is chaotic and dominated by finer spatial scales. In contrast, $m = 1a$ (the cosine coefficient) has a more organized structure, with greater fluctuation magnitudes, which reflect the dominance of flapping motions along the minor axis plane. This is the primary instability mechanism of rectangular and elliptical jets as shown by theoretical [69] and

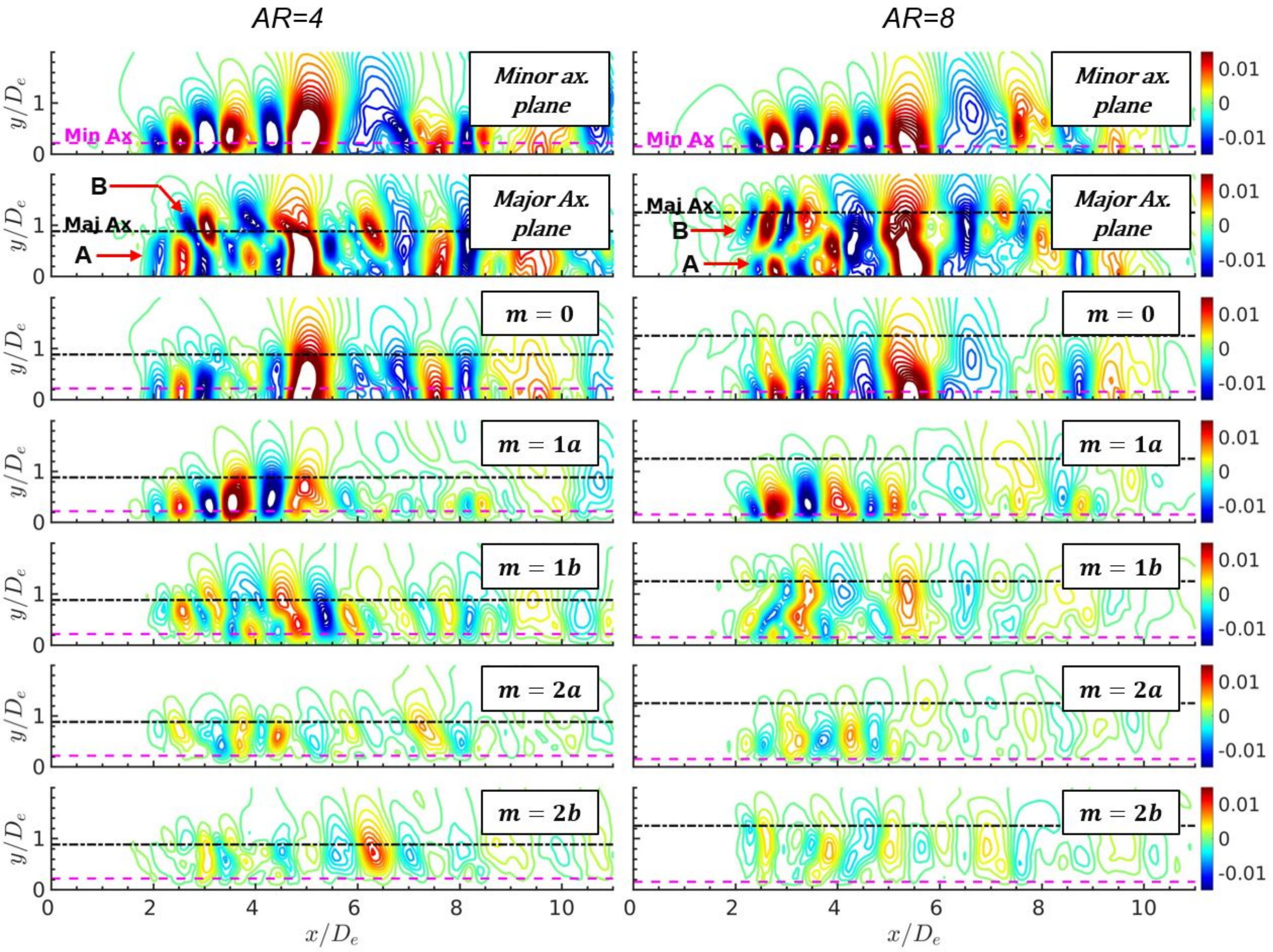

FIG. 10: Contours of streamwise acoustic fluctuations ($\frac{\partial \psi'_A}{\partial x}$) of the $AR = 4$ (left column) and $AR = 8$ (right column) jets shown on the major and minor axis planes along with the leading azimuthal Fourier modes

experimental [27, 28] studies. The manifestations of these differences between the two coefficients of the first mode on the near-acoustic field asymmetry are discussed in a subsequent section. The coefficients of the second mode $m = 2a$ and $2b$, however, exhibit more chaotic structures that do not resemble the fluctuation pattern on either of the symmetry planes of the jets. This is consistent with the higher complexity of the $m = 2$ mode discussed in the context of fig. 7.

### C. 3D reconstruction of modes

Overall, both circular and rectangular jets display similar decreases in the fluctuation magnitudes of the higher azimuthal modes. The greater influence of lower modes suggests that procedures developed for circular jets, that consider only a few dominant Fourier modes, may also apply to high $AR$ rectangular jets. This convergence of instantaneous statistics in the azimuthal Fourier space, as well as the dynamics of the individual modes, is now clarified by considering 3D reconstructions of the leading azimuthal modes. Qualitative considerations are presented first, followed by more quantitative evaluations.

3D mode shapes are reconstructed using the 2D Fourier coefficients ($p_a^m(r, x, t)$ and $p_b^m(r, x, t)$) and their corresponding azimuthal variations ($\cos m\phi$ and $\sin m\phi$) according to equation 12. Figure 11 shows the instantaneous 3D snapshots of the three leading rectangular jet azimuthal modes using iso-surfaces of the same value ($\frac{\partial \psi'_A}{\partial x} = \pm 0.007$) and compares them to those of the circular jet. For the $AR = 1$ jet, a steep drop in higher azimuthal mode content is evidenced by the reduced spatial support of the iso-surfaces and the higher azimuthal modes become further restricted

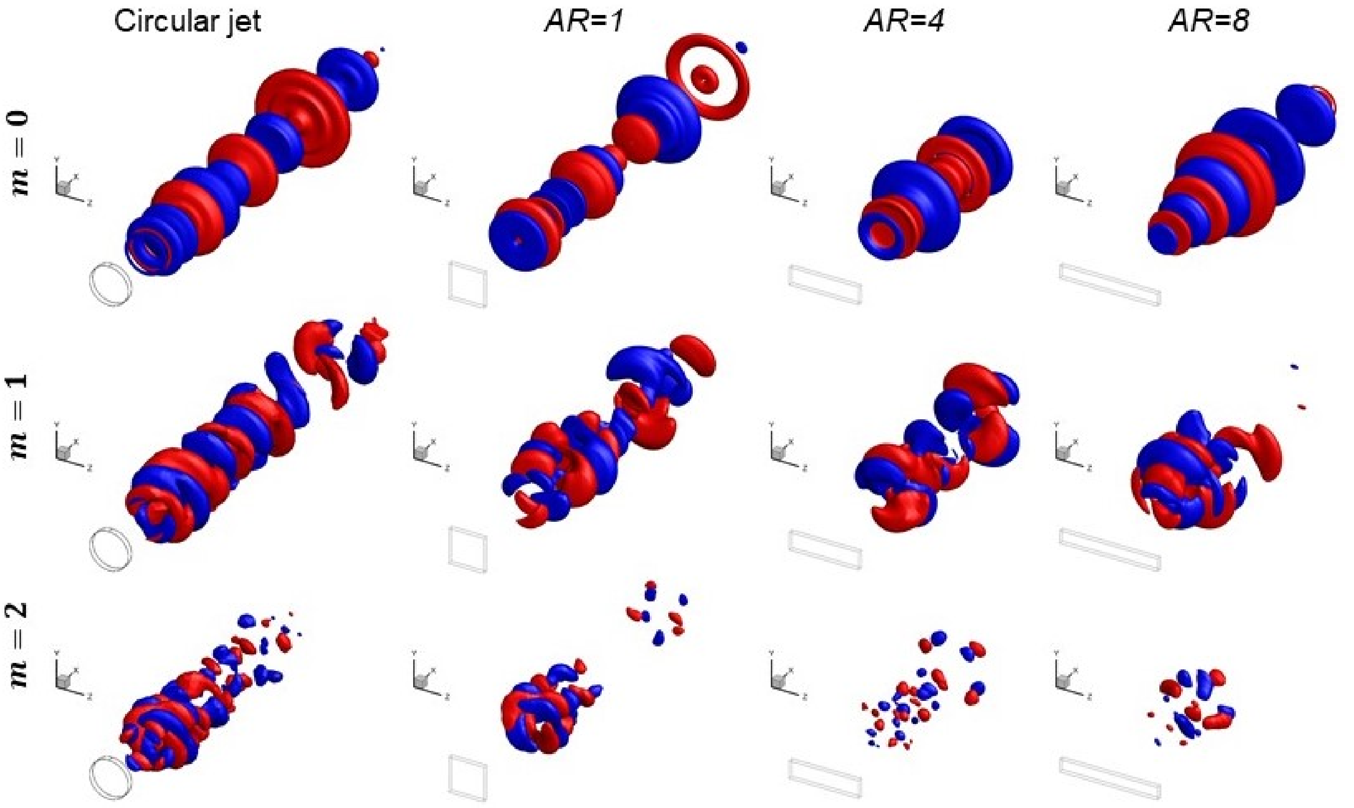

FIG. 11: Iso-surfaces ($\frac{\partial \psi'_A}{\partial x} = \pm 0.007$) showing the reconstructed 3D azimuthal mode shapes of an instantaneous snapshot of the acoustic fluctuations in the nearfield of the various $AR$ jets

to the near nozzle regions. These observations are quite similar to those by Cavalieri *et al.* [70] in the context of the higher azimuthal modes of circular jets. This reiterates a crucial observation, since the streamwise non-compactness of the acoustic source field is a necessary criterion for superdirective acoustic radiation from a jet [19, 21].

More interestingly, despite the persistent mean asymmetry of the higher $AR$ jets, their higher azimuthal modes (fig. 11) also show similar characteristics and indeed, an even steeper drop off in amplitudes. This observation is associated with the relative simplicity of the acoustic fluctuations in the high $AR$ rectangular jets (fig. 6 second row), compared to the hydrodynamic content of the turbulent eddies (fig. 6 third row). While the former is spatially localized with distributions that are relatively independent of the $AR$, the latter clearly highlights the greater spreading rate and the more chaotic nature of the higher $AR$ jets. The 3D mode shapes at higher $AR$ also further highlight the progressively diminishing streamwise extent of the azimuthal modes of the rectangular jets compared to the circular jet as discussed previously in the context of the 2D Fourier coefficients. These results show promise regarding the potential suitability of the cylindrical coordinate system, and by extension the Fourier basis in the azimuthal direction, in describing the instantaneous dynamics of rectangular jets.

As an additional qualitative assessment, the compact support in the chosen Fourier basis is evaluated by reconstructing the flow using only a few leading modes. A partial reconstruction considering only the leading $M$ azimuthal modes is obtained from:

$$\hat{q}_M(x,r,\phi,t) = \sum_{m=0}^{M} q_a^m(x,r,t)cos(m\phi) + q_b^m(x,r,t)sin(m\phi) \tag{15}$$

These partial reconstructions are compared with the instantaneous fluctuation snapshot of the $AR = 8$ rectangular jet in fig. 12. The first row of fig. 12 shows the partial reconstructions of $\frac{\partial \psi'_A}{\partial x}$ using progressively larger numbers of azimuthal modes up to $M = 5$. The original 3D snapshot of acoustic fluctuations is repeated below each partial reconstruction for comparison purposes in the second row. The reconstruction error is obtained as the difference between the partial reconstruction and the LES snapshot:

$$\epsilon_M(x,r,\phi,t) = q(x,r,\phi,t) - \hat{q}_M(x,r,\phi,t) \tag{16}$$

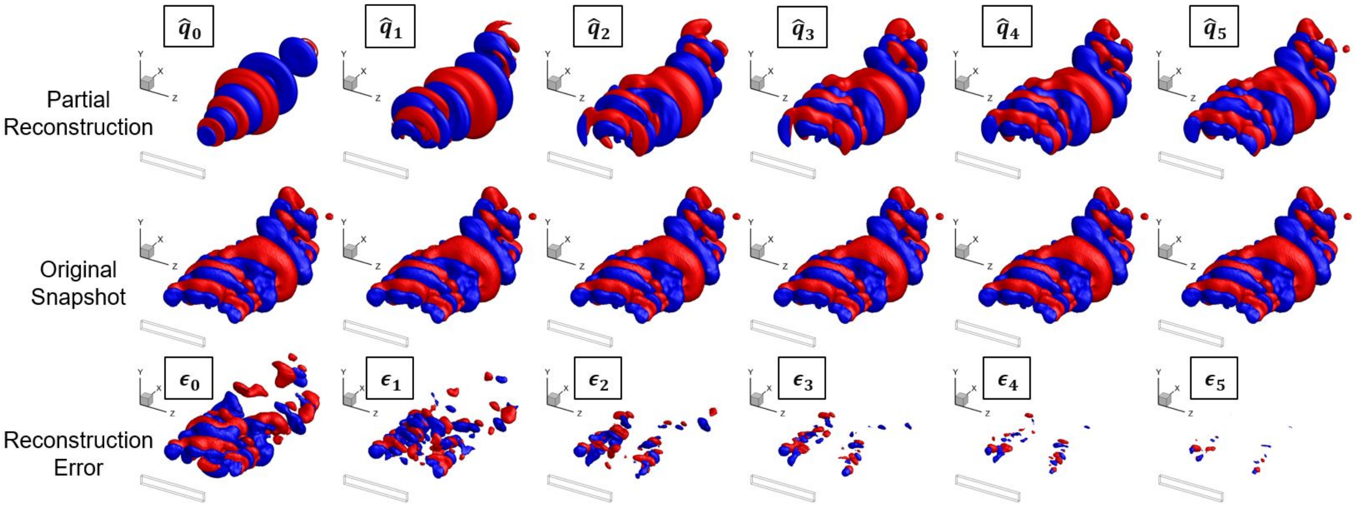

FIG. 12: A comparison of partial reconstructions using a few leading azimuthal modes to the original instantaneous snapshot of the acoustic fluctuations in the $AR = 8$ rectangular jet. The reconstruction error for each of the partial reconstructions is also shown

is plotted in the third row of fig. 12. The reconstruction error decreases rapidly with $M$, evident from the close correspondence between the five mode reconstruction ($\hat{q}_5$) and the original snapshot. Similar results for the $AR = 4$ jet are shown in Chakrabarti *et al.* [37] Interestingly, with the consideration of additional modes, the streamwise extent of the reconstruction error also reduces rapidly and the error is restricted to only the near nozzle regions for reconstructions with four or five azimuthal modes.

### D. RMS reconstruction accuracy

A quantitative assessment of the reconstruction is performed to compare the convergence rates of the azimuthal Fourier series for different $AR$s, as well as to differentiate between the rates of convergence of $p'$ and $\frac{\partial \psi'_A}{\partial x}$ for a given jet. A meaningful comparison is predicated on an appropriate error norm; here we choose the volume integrated mean square error given as:

$$||\epsilon_M|| = \frac{\int_V \frac{1}{T}\int_0^T \epsilon_M(x,r,\phi,t)^2 dtdV}{\int_V \frac{1}{T}\int_0^T q(x,r,\phi,t)^2 dtdV} \tag{17}$$

The denominator is the RMS of the fluctuation field being analyzed; it normalizes the error to yield the fraction of the total fluctuation energy of the field. The volume of integration is a cylinder containing all acoustically significant regions within the jet. Thus, the streamwise and radial extents are $x/D_e = 25$ and $3D_e$, respectively, which coincides with the radial location of the FWH surface.

Figure 13 compares the reconstruction error norm as a function of number of modes used for reconstruction for the $AR = 4$ and $AR = 8$ rectangular jets with the reference results for the circular jet. The error norm decreases with number of modes as anticipated. In each case, the axisymmetric mode of $\frac{\partial \psi'_A}{\partial x}$ exhibits a lower reconstruction error than $p'$ and the error drops at a sharper rate, indicating a more rapid convergence in the azimuthal Fourier space. To highlight this, the figures also include a plot of the $\frac{\partial \psi'_A}{\partial x}$ error, shifted to match the pressure fluctuation reconstructions errors for $m = 0$ alone. Thus, the acoustic fluctuations, exhibit lower-rank behaviour in azimuthal Fourier space with lower reconstruction errors compared to the pressure fluctuations. This confirms that the advantage of employing the acoustic fluctuations instead of the raw pressure fluctuation field in circular jets carries over to rectangular jets.

Second order statistics provide further insights into the behavior of the individual Fourier modes in establishing the acoustic field. The modal energies (mean squared magnitudes) of the leading azimuthal Fourier modes are defined as:

$$q_m^{MS}(x,r) = \begin{cases} \overline{q_{a0}^2} & \text{if } m = 0 \\ \frac{\overline{q_{am}^2 + q_{bm}^2}}{2} & \text{if } m > 0 \end{cases} \tag{18}$$

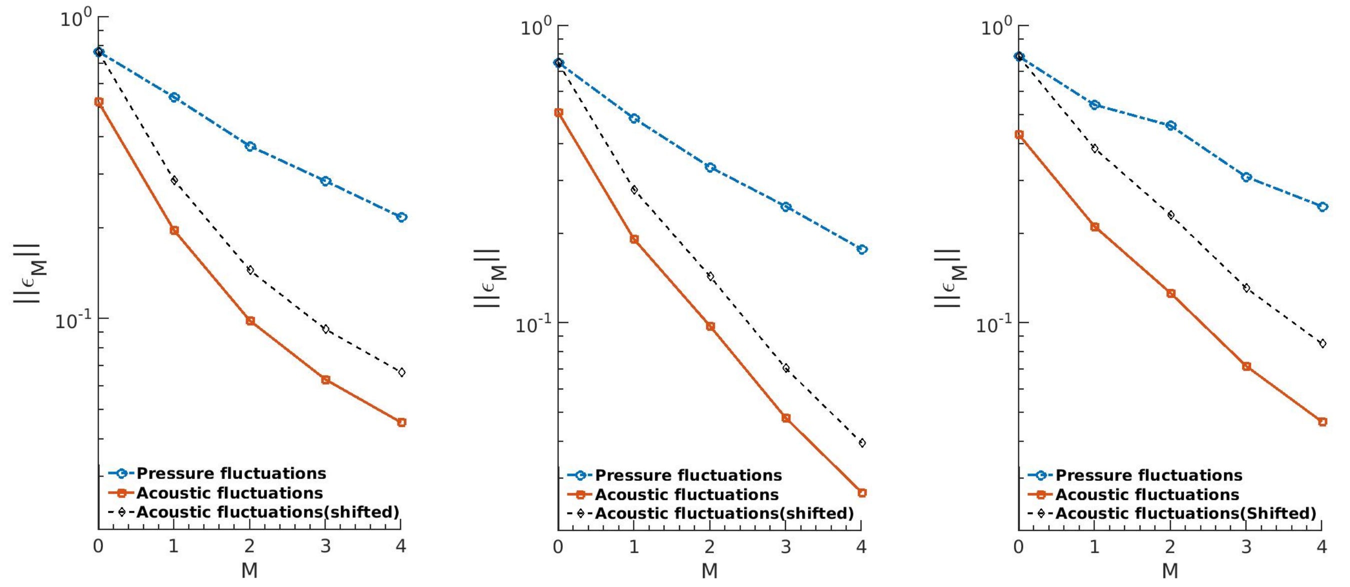

(a) Equivalent circular jet

(b) AR=4

(c) AR=8

FIG. 13: Comparison of the rates of convergence for the circular jet (a), $AR = 4$ (b), and $AR = 8$ (c) rectangular jets

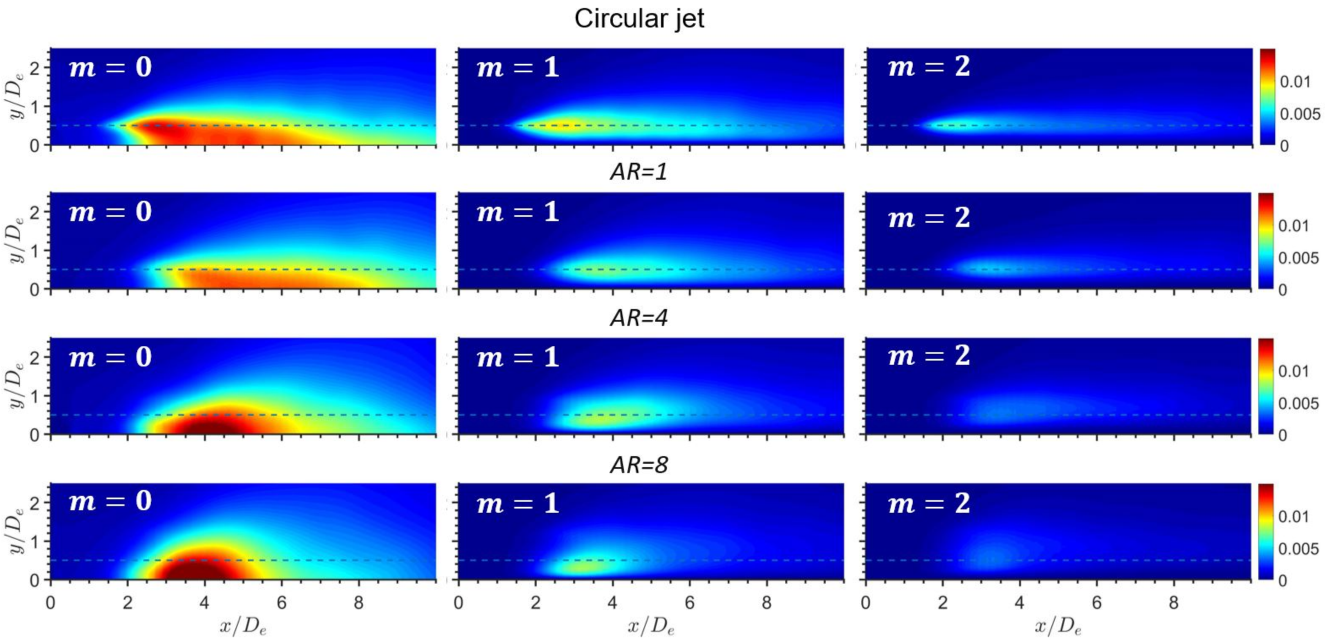

FIG. 14: Modal energies of the three leading azimuthal modes of the acoustic fluctuations in the non-axisymmetric jets. The dashed line in the figure represents the lipline of the circular jet ($y/D_e = 0.5$) for scale

For completeness, a derivation of the above expression is given in appendix A (equation A6). A similar definition for the modal energies has been adopted by Faranosov *et al.* [71].

Figure 14 compares the spatial energy distribution of the leading azimuthal modes of $\frac{\partial \psi'_A}{\partial x}$ in the different jets. The circular jet (fig. 14 first row) clearly exhibits the two major trends of decreasing modal energy and diminishing spatial support with increasing mode numbers, which have facilitated reduced order modeling. Results for rectangular jets (third and fourth rows) also confirm the progressively smaller energies of the higher azimuthal modes, at rates that are generally commensurate with those for the circular jet. Thus, the property of rapid convergence of statistics

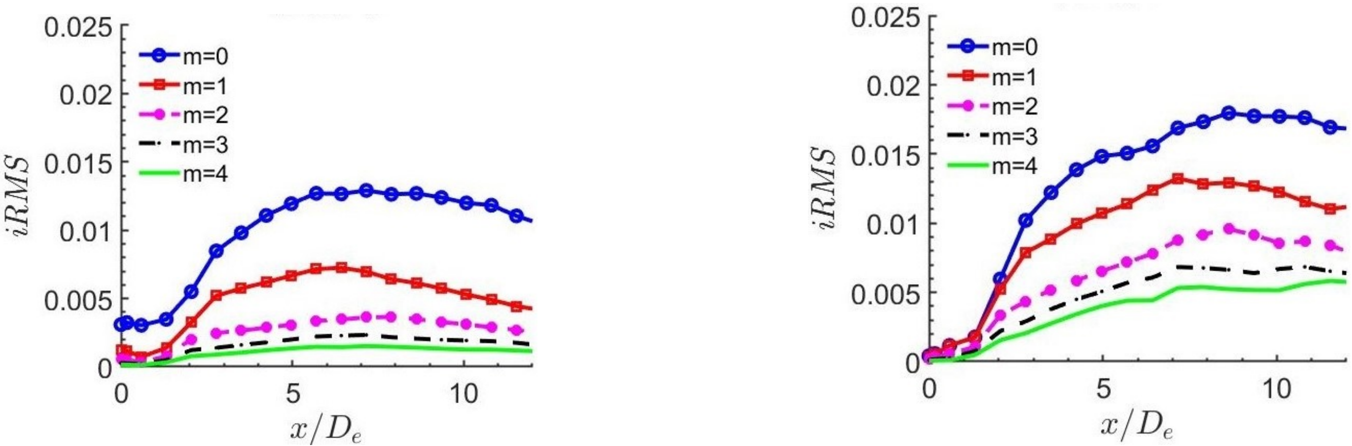

(a) $\frac{\partial \psi'_A}{\partial x}$

(b) $p'$

FIG. 15: Streamwise variation of the radially integrated modal energies of five leading azimuthal modes for the circular jet

with number of modes holds even for high $AR$ rectangular jets which display features such as axis-switching. Two trends of interest may be identified. First, modal energies exhibit a greater radial spread with increasing $AR$; this is most evident from a comparison of the $m = 0$ energy distribution at the lipline (marked with a dashed line) of the circular jet ($y/D_e = 0.5$). This is consistent with the azimuthal averaging effect; the major axis shear layers are geometrically further away from the axis, similar to the effect in fig. 10. The second trend concerns the decrease in the streamwise extent of all azimuthal modes with increase in the $AR$, again most clearly evidenced by the marked decrease in the streamwise extension of the $m = 0$ mode of the $AR = 8$ jet (see the first column of fig. 14). It has been previously shown in the context of circular jets [11] that the streamwise extent of the acoustic sources is correlated with the length of the potential core. This result holds for rectangular jets as well, since the decrease in the streamwise length-scale of the acoustic sources [39] of the high $AR$ jets is correlated with a progressive reduction in their potential core lengths of the higher $AR$ rectangular jets (fig. 4).

A suitable measure for a direct quantitative comparison of modal energies may be obtained as follows. Since the radial distributions of modal energies vary with $AR$, comparing the energy magnitudes along a specific streamwise line (as is common in circular jets) is not illuminating. This is evident from the fig. 14, where the dashed lines in the figures mark the radial distance corresponding to the lipline of the circular jet ($r = 0.5D_e$). In contrast to the circular jet, where most of the energy for all azimuthal modes is concentrated around the $r = 0.5D$ line, higher $AR$ jets exhibit a significantly greater spatial spread with only a fraction of the energy being contained along the $r = 0.5D_e$ line. An integrated measure of energy magnitude, $q_m^{iMS}$, with radial distance at each axial station is thus employed:

$$q_m^{iMS}(x) = \int_0^3 q_m^{MS}(x, r) r dr \tag{19}$$

where $q$ is the flow variable of interest ($\frac{\partial \psi'_A}{\partial x}$ or $p'$). The radial domain of integration is again chosen from the axis to $r = 3D_e$, which is the location of the FWH surface and is sufficiently distant from the turbulent core for all modal energies to have decreased by two orders of magnitude.

Figure 15 shows the integrated energies of the leading azimuthal modes of (a) together with corresponding results for $p'$ (b) of the circular jet for reference. Near the nozzle exit, the separation of the energies between the azimuthal modes is quite small for pressure, but not so for the acoustic component, whose $m = 0$ content is already much larger than the others. Further downstream, the content of all modes increases; however, the increase is largest for the lower modes. This reiterates the low-rank nature of fluctuation statistics in the azimuthal Fourier space and, therefore, a rapid convergence in the three leading azimuthal modes. Figure 15 quantifies some of the previously noted features and distinctions between pressure and acoustic fluctuations. While all azimuthal modes of $\frac{\partial \psi'_A}{\partial x}$ exhibit clear growth and subsequent decay with streamwise distance, the integrated modal energies of $p'$ continue to increase for much longer streamwise distances. This growth and decay envelope of acoustic fluctuations reveals a characteristic streamwise acoustic source length-scale, which is a critical component of jet acoustic emissions, as discussed in Unnikrishnan *et al.* [39]. Further, acoustic fluctuations exhibit a more rapid convergence in the azimuthal Fourier space as manifested by the larger differences in modal energies with increasing mode numbers, most evident around $x/D_e = 5$. Azimuthal modes of $p'$ do not show as pronounced a drop-off in energy.

The convergence properties of $\frac{\partial \psi_A'}{\partial x}$ are inherent in the defining Poisson equation 7, whose solution may be distinguished into homogeneous and particular components. The homogeneous solution component is relatively small, since it depends on relatively distant far field boundary conditions, where $\psi_A = 0$. The particular solution component is dependent on the nature of the source term, which connects pressure fluctuations, $\partial p'/\partial t$, to the acoustic potential, $\psi_A$, and may be analyzed in Fourier space. To illustrate in two-dimensions $(x - \theta)$ for simplicity, equation 7 may be written in cylindrical coordinates as:

$$\frac{1}{r^2}\frac{\partial^2 \psi_A}{\partial \theta^2} + \frac{\partial^2 \psi_A}{\partial x^2} = -\frac{1}{c^2}\frac{\partial p'}{\partial t} \tag{20}$$

or, in wavenumber-frequency space,

$$\left(\frac{m^2}{r^2} + k_x^2\right)\widehat{\psi}_A = -\frac{\omega}{c^2}\widehat{p'} \tag{21}$$

where $\widehat{\psi}_A(k_r, k_x, m, \omega)$ is the Fourier transform of $\psi_A$. $\widehat{\psi_A}$ is thus directly dependent on $\widehat{p'}$ by a wavenumber-dependent scaling factor.

$$\widehat{\psi}_A = -\frac{\omega}{c^2}\frac{\widehat{p'}}{\left(\frac{m^2}{r^2} + k_x^2\right)} \tag{22}$$

In the quiescent farfield, where the speed of sound is constant, this relationship is greatly simplified [72]. While the connection is not as straightforward in the nearfield, a key observation is that as the radial distance decreases, the sensitivity of this relationship to azimuthal wavenumbers increases. Near the centerline of the jet, the higher azimuthal modes have very low weights as the quantity $m^2/r^2$ in denominator becomes large. In this region, therefore, the acoustic fluctuations filter out the higher azimuthal modes that may dominate the fully turbulent dynamics, *i.e.,* including non-acoustic components. Moving radially outward from the jet, the higher azimuthal modes are dissipated faster owing to the physics of acoustic propagation. The combined result of these two effects manifests in the superior convergence of the acoustic fluctuations in the azimuthal Fourier spectrum when compared to the pressure fluctuations.

The integrated modal energies of $\frac{\partial \psi_A'}{\partial x}$ and $p'$ for the rectangular jets are compared in fig. 16. The same trends as observed for the circular jets persist; in particular, the energy content decreases for higher mode numbers. As such, acoustic fluctuations of even high $AR$ rectangular jets have appreciably low rank representation in the azimuthal Fourier basis. This result further verifies the observation that despite the non-axisymmetric nature of the rectangular nozzle plume, significant simplifications of the rectangular jet may be achieved by considering only the leading azimuthal Fourier modes, especially if $\frac{\partial \psi_A'}{\partial x}$ is employed instead of $p'$ as discussed previously in the context of fig. 13. Additionally, with increasing $AR$, (i) the $m = 0$ mode becomes relatively more energetic compared to $m = 1$ and (ii) for all azimuthal mode numbers, the streamwise location corresponding to the peak value of the RMS shifts progressively upstream and the post-peak reduction becomes steeper, especially when compared to the circular jet, consistent with the decrease in potential core length with $AR$.

## VI. AZIMUTHAL HOMOGENEITY CONSIDERATIONS

The fluctuations in an azimuthal Fourier basis retain the rapid convergence property even for rectangular jets, implying that despite their higher complexity, the cylindrical coordinates are well suited to represent their acoustic dynamics. However, as noted earlier in the context of the mean flow description, rectangular jets exhibit several differences from circular jets, including axis-switching and non-axisymmetric farfield radiation. Given the relatively negligible contribution of the higher azimuthal Fourier modes in all of the jets, these differences between the dynamics of high $AR$ rectangular and circular jets can only be associated with key differences in the dynamics of the leading azimuthal modes. Indeed, a major point of distinction between circular and rectangular jets is that the former exhibit azimuthal statistical homogeneity that greatly simplifies their modeling [14, 15, 19]. This section examines the advantages afforded by the azimuthal homogeneity property in the context of the chosen Fourier decomposition ansatz, and evaluates its applicability to rectangular jets.

The implication of azimuthal homogeneity in the context of Eq. 12 may be examined in the simpler notation that suppresses explicit $x$ and $r$ dependence:

$$q(\phi, t) = a_0(t) + \sum_{m=1}^{\infty} a_m(t)\cos m\phi + b_m(t)\sin m\phi \tag{23}$$

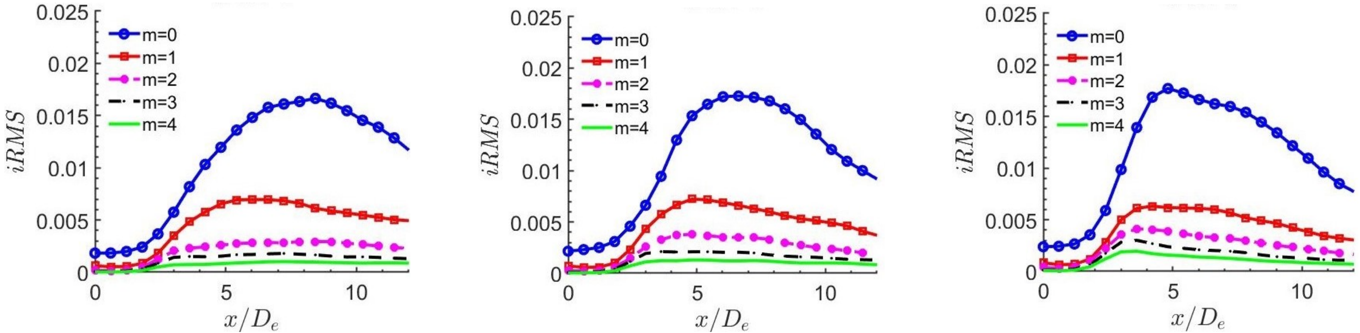

(a) $AR = 1$ $\frac{\partial \psi'_A}{\partial x}$ (b) $AR = 4$ $\frac{\partial \psi'_A}{\partial x}$ (c) $AR = 8$ $\frac{\partial \psi'_A}{\partial x}$

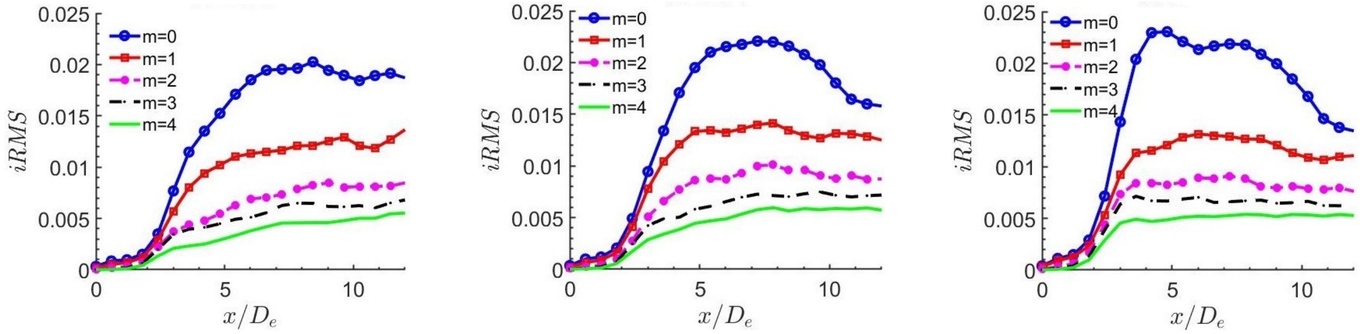

(d) $AR = 1$ $p'$ (e) $AR = 4$ $p'$ (f) $AR = 8$ $p'$

FIG. 16: Streamwise variation of the radially integrated RMS (iRMS) of the five leading azimuthal modes of the acoustic (row 1) and pressure fluctuations (row 2) for the $AR = 1$ (a,d), $AR = 4$ (b,e), $AR = 8$ (c,f) jets

Homogeneity in the $\phi$ direction requires that the two point cross-correlation function depend only on the angular separation, $\Delta\phi = \phi_1 - \phi_2$, and not on $\phi$ itself [14]:

$$\overline{q(\phi_1, t)q(\phi_2, t)} = g(\phi_1 - \phi_2) \tag{24}$$

Here, $\overline{(.)}$ refers to an averaging operation in time. A direct consequence of this, as shown in Appendix A, is that the individual Fourier modes obey the following constraints:

$$\overline{a_m^2} = \overline{b_m^2} \tag{25}$$

$$\overline{a_m a_n} = \overline{b_m b_n} = \overline{a_m b_n} = 0 \tag{26}$$

These may be interpreted by considering the sense of direction associated with the azimuthal modes, based on the locations of the extrema of the sine and cosine functions, as discussed in the context of fig. 7. The first constraint (equation 25), therefore, reflects the polar symmetry property of circular jets; specifically, both cosine and sine coefficients ($a_m$ and $b_m$ respectively) have identical statistics due to azimuthal statistical invariance.

The second constraint (equation 26) reflects the property that in the homogeneous and periodic direction, the Fourier modes diagonalize the cross correlation matrix and are the spatial POD modes [15]. As a result, the decomposition equation 23 has correspondence to the space-time variable separation achieved by POD, where the sine and cosine functions represent the spatial POD modes and are mutually orthogonal in space by construct. By extension, the Fourier coefficients ($a_m$ and $b_m$), correspond to the temporal POD modes and must be mutually orthogonal in time, as indicated by the above noted constraint.

These properties have simplified circular jet noise modeling efforts. For instance, POD analyses of the individual azimuthal modes (instead of the full 3D dataset) are routinely used to develop reduced-order models [6, 20]. The calculation of OASPL levels using azimuthal modes is also simplified because the mutual incoherence of the individual azimuthal modes dictated by the statistical homogeneity (equation 26) permits fluctuation RMS value to be represented as the sum of squares of the RMS values of the individual azimuthal Fourier modes [15, 19]. Thus, by considering only the three leading modes for a circular jet, the energy of the overall fluctuation field is given as (see appendix A):

$$\overline{q^2(\phi,t)} = \overline{a_0^2} + \frac{\overline{a_1^2} + \overline{b_1^2}}{2} + \frac{\overline{a_2^2} + \overline{b_2^2}}{2} \tag{27}$$

The azimuthal invariance of the fluctuation RMS value, as evidenced by the absence of the azimuthal angle $\phi$ on the RHS of the above expression, implies that even if infinitely many azimuthal modes are considered, the overall RMS of the fluctuations retain their axisymmetric form for a circular jet [15].

These considerations do not hold when two point correlations depend on the azimuthal angle; for example, in the case of a rectangular jet, the correlation between points on the y ($\phi = 0^o$) and z ($\phi = 90^o$) axes (fig. 5a) respectively, display different correlations with each other than those along $\phi = 45^o$ and $\phi = 135^o$. This aspect manifests in the near and farfield asymmetry of the rectangular jet dynamics, regardless of the rapid convergence in the azimuthal Fourier basis shown previously. A generalized expression for the fluctuation RMS, applicable for azimuthally non-homogeneous data, may be written as a function of the individual modal contributions as follows (derivation in appendix (equation A5)):

$$\begin{aligned}\overline{q^2(\phi,t)} = {} & \overline{a_0^2} + \frac{\overline{a_1^2} + \overline{b_1^2}}{2} + \frac{\overline{a_2^2} + \overline{b_2^2}}{2} \\ & + \frac{\overline{a_1^2} - \overline{b_1^2}}{2}\cos 2\phi + \frac{\overline{a_2^2} - \overline{b_2^2}}{2}\cos 4\phi \\ & + 2\overline{a_0 a_1}\cos\phi + 2\overline{a_0 b_1}\sin\phi + 2\overline{a_0 a_2}\cos 2\phi + 2\overline{a_0 b_2}\sin 2\phi \\ & + 2\overline{a_1 b_1}\sin\phi\cos\phi + 2\overline{a_1 a_2}\cos\phi\cos 2\phi + 2\overline{a_1 b_2}\cos\phi\sin 2\phi \\ & + 2\overline{b_1 a_2}\sin\phi\cos 2\phi + 2\overline{b_1 b_2}\cos\phi\sin 2\phi + 2\overline{a_2 b_2}\cos 2\phi\sin 2\phi\end{aligned} \tag{28}$$

The complications associated with lack of homogeneity require consideration of additional terms to account for the inequality of sine and cosine coefficients ($\frac{\overline{a_m^2} - \overline{b_m^2}}{2}$) as well as modal interactions ($\overline{a_m a_n}$), that must be modeled.

The generalized RMS expression (equation A5) aids in identifying physical mechanisms related to azimuthal inhomogeneities and asymmetry. For example, the term $\frac{\overline{a_1^2} - \overline{b_1^2}}{2}$ is related to the dominance of flapping motions along the major or minor axes planes. This is linked to the directivity given by $\cos 2\phi$ and is visualized in fig. 7c. Thus, the dominance of flapping motions along one axis results in the increase of the RMS in that direction and a reduction on the other axis.

Equation 28 is generalized and does not take into account the specifics of the problem. Some simplification is afforded by exploiting horizontal and vertical symmetry of rectangular jets about the minor and major axes respectively. The directivity of their radiation can then only assume azimuthal harmonics of the form $2n\phi$. To elucidate this point, the coupling between the axisymmetric and first azimuthal mode is reflected in the term $2\overline{a_0 a_1}\cos\phi$, whose associated directivity, given by $\cos\phi$, is shown graphically in fig. 7a. This yields an increase in acoustic intensity on one side of the minor axis plane of the jet along with a reduction on the other, violating the underlying symmetry of the problem. Further, among the even harmonics, the sine function ($\sin 2n\phi$) results in a spatial variation that is antisymmetric about the major and minor axis planes of symmetry. Thus, by exploiting the symmetry of the rectangular jet problem, all terms resulting in directivities given by odd harmonics in $\phi$ as well as those containing even harmonics of the sine function may be removed from the expression. This simplification is a direct result of the choice of the particular ansatz for the Fourier decomposition used in this study (equation 12). Thus, the simplified expression for the fluctuation RMS is given by:

$$\begin{aligned}\overline{q^2(\phi,t)} = {} & \overline{a_0^2} + \frac{\overline{a_1^2} + \overline{b_1^2}}{2} + \frac{\overline{a_2^2} + \overline{b_2^2}}{2} \\ & + \frac{\overline{a_1^2} - \overline{b_1^2}}{2}\cos 2\phi + \frac{\overline{a_2^2} - \overline{b_2^2}}{2}\cos 4\phi + 2\overline{a_0 a_2}\cos 2\phi\end{aligned} \tag{29}$$

The terms related to azimuthal inhomogeneity are evaluated for the three non-axisymmetric jets in fig. 17. The modal energy of the leading $m = 0$ mode is also shown (first row) to highlight the importance of inhomogeneous processes relative to the dominant acoustic sources. Clearly, one of the most important contributors to the asymmetry are the differences between the sine and cosine coefficients of the first azimuthal mode (modes $1a$ and $1b$). The preferential flapping in the minor axis direction noted in the context of fig. 10 manifests in larger values for $\overline{a_1^2}$ compared to $\overline{b_1^2}$. Indeed, in rectangular jets, the cosine and sine coefficients ($a_1$ and $b_1$ respectively) represent distinct physical processes on the major and minor axis planes. The preferential growth of instabilities and flapping motions

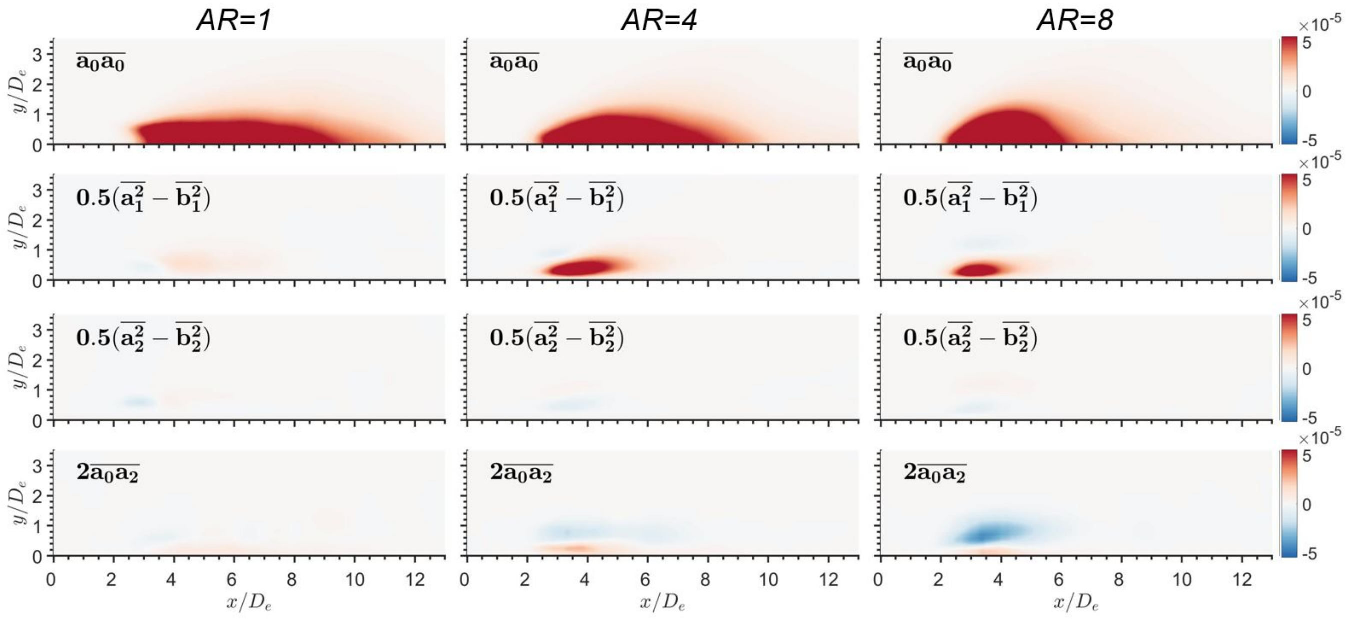

FIG. 17: Contours showing the leading $m = 0$ azimuthal mode and spatial distributions of the dominant terms associated with azimuthal inhomogeneity and acoustic radiation asymmetry for all simulated rectangular jets

along the minor axis plane has been shown to be a dominant dynamic feature of higher $AR$ rectangular jets, and hypothesized as a cause of asymmetries in the farfield acoustic radiation of jets [62]. In addition to the above, the $AR = 8$ jet also exhibits a coupling between the axisymmetric and second azimuthal mode ($\overline{a_0a_2}$) although it is much weaker than the flapping mechanism.

Other important features evident in fig. 17 may be summarized as follows. The preferential flapping motions manifested in the disparity between the sine and cosine coefficients of $m = 1$ ($\overline{a_1^2} - \overline{b_1^2}$) occurs over a larger spatial spread for the $AR = 4$ jet compared to the $AR = 8$ jet. This is similar to the reduction in the streamwise length-scale of the higher $AR$ jets due to a reduction in the potential core length. However, in both these rectangular jets, the relative magnitudes and spatial spread of the flapping motions are much smaller compared to the $m = 0$ azimuthal mode ($\overline{a_0a_0}$). Furthermore, the square jet, shows a very small difference between the two coefficients of the first mode. This is due to the added symmetry of the problem *i.e.,* in addition to symmetry about the major and minor axes, the square ($AR = 1$) jet is also symmetric along its diagonals (four fold mirror symmetry). Thus, any departure from axisymmetry for the square jet must be of the form $\cos 4n\phi$. Preferential flapping along either of the planes bisecting the sides in a square jet would result in an unacceptable asymmetry given by $\cos 2\phi$. Interestingly, several terms that are not identically zero in square jets are found to be negligible, for example, $\overline{a_2^2} - \overline{b_2^2}$, which would result in a fourth harmonic in the azimuthal direction. This is consistent with the axisymmetric farfield acoustic radiation obtained for the case of the square jet.

## VII. REDUCED NEARFIELD MODEL

The above findings may be used to inform a reduced order model for the non-axisymmetric nearfield of rectangular jets; for completeness the corresponding results for circular jets are also presented. Figure 18 displays the polar plot distribution of azimuthal acoustic fluctuation RMS on the FWH surface for the circular (a) and the $AR = 8$ (b) rectangular jets at the streamwise location of $x/D_e = 5$, which corresponds to the peak acoustic radiation (in the downstream shallow angle direction). As anticipated, the circular jet exhibits no variation in acoustic intensity with respect to the azimuthal angle. In this case, due to the azimuthal homogeneity, the overall RMS obtained from the LES can be faithfully reproduced by directly adding the modal energies of the individual azimuthal modes per equation 27. The cumulative sum of the modal energies of the four leading azimuthal modes is shown using dashed black lines. The $m = 0$ energy, shown by the dotted line, closest to the center of the plot accounts for 78% of the observed acoustic intensity. The sum of the two leading modes, namely $m = 0$ and $m = 1$, constitutes 94% of the total acoustic intensity and is quite close to overall RMS observed from the LES. Adding higher azimuthal modes progressively recovers the LES results; for example, the sum of the first 3 azimuthal modes *i.e.* $\Sigma m = 2$) yields 97%

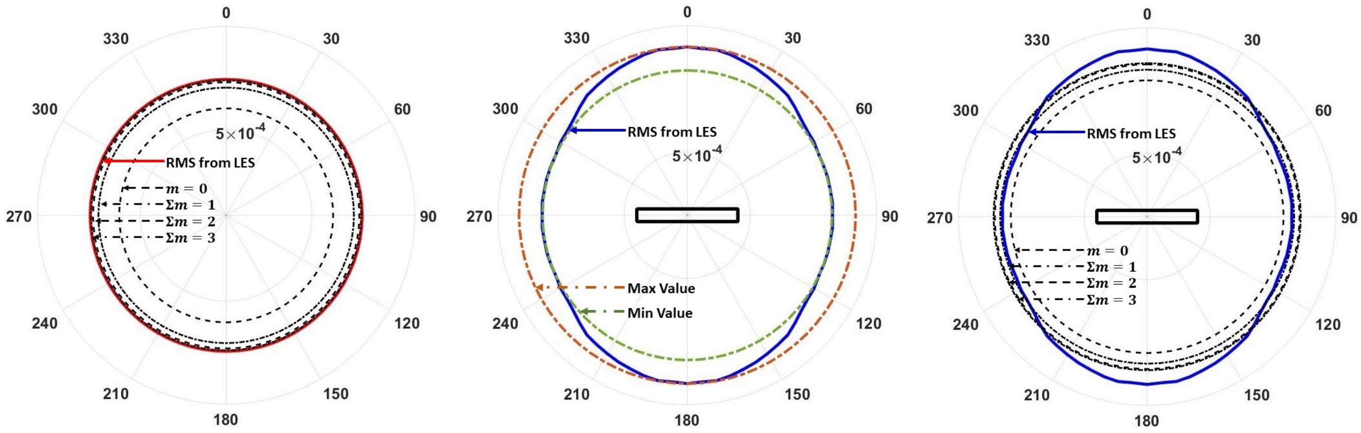

(a) Reconstruction of circular jet acoustics assuming azimuthal homogeneity

(b) $AR = 8$ jet acoustic intensity highlighting nearfield asymmetry

(c) $AR = 8$ jet nearfield reconstruction assuming azimuthal homogeneity

FIG. 18: Azimuthal distributions of the acoustic intensity on the FWH surface at the streamwise location of the maximal jet noise shown using polar plots for the circular and $AR = 8$ rectangular jets. Reconstructions of the acoustic intensity using the cumulative sum (equation 27) of the $m$ leading modal energies (indicated by the $\sum m$ value) are shown for both jets

of the observed acoustic intensity. However, higher modal contributions diminish in consistency with the above noted rapid convergence of fluctuation statistics.

Figure 18b shows the azimuthal variation of the nearfield acoustic intensity of the $AR = 8$ jet to highlight its nearfield asymmetry. A schematic of the nozzle exit is also shown for orientation. A peak in the acoustic intensity is distinctly visible on the minor axis plane which was shown previously (section III) to be the direction of the maximum acoustic intensity of the $AR = 8$ jet. The difference between the minimum and maximum acoustic intensity (shown in the figure using green and orange dashed lines) is about 15% of the average RMS around the azimuth. Bridges [31], Kantola [62] also observed the minor axis plane of high $AR$ rectangular jets to be louder. Figure 18c shows reconstructions of the nearfield acoustic intensity of the rectangular jet following a procedure similar that used for the circular jet in fig. 18a, *i.e*, using equation 27. This approach fails to capture the nearfield asymmetry of the rectangular jet and results in under and overpredictions along the major and minor axis directions, respectively.

Thus, the terms associated with non-homogeneity, discussed in section VI, are crucial to the reconstruction of the higher aspect ratio rectangular jets. This is shown in fig. 19 for all the non-axisymmetric jets. The nearfield asymmetry of $AR = 8$ (fig. 19c.) is recovered by adding only two additional terms associated with inhomogeneity in equation 29: $0.5(\overline{a_1^2} - \overline{b_1^2})\cos 2\phi$ and $\overline{a_0 a_2}$, incorporating preferential flapping and the coupling of the axisymmetric and second azimuthal modes, respectively. This corrected reconstruction shown using the magenta hatched line successfully reproduces the asymmetry in the nearfield acoustic intensity. A similar situation is also visible for the $AR = 4$ jet (fig. 19b).

Interestingly, in line with its overall similarity to the circular jet, the square jet exhibits an azimuthally uniform nearfield acoustic intensity (fig. 19a). As a result, a nearfield acoustic reconstruction assuming azimuthal homogeneity (following equation 27) gives a close approximation of the measured acoustic field. Adding the terms related to the inhomogeneity has a negligible effect on the reconstruction. This is consistent with the relatively negligible magnitudes of the inhomogeneity terms in the square jet (as shown in fig. 17).

The nearfield RMS acoustic intensity for $AR = 4$ and $AR = 8$ jets display preferential flapping along the minor axis direction $(0.5(\overline{a_1^2} - \overline{b_1^2})\cos 2\phi)$; this is the dominant mechanism related to the nearfield asymmetry as evidenced by fig. 17. The differences between the $AR = 4$ and $AR = 8$ jets may be highlighted by examining the flapping term in both as a fraction of the axisymmetric modal energy. Figure 20 shows the importance of the primary term representing flapping for both the $AR = 4$ and $AR = 8$ jets along a ray following the direction of maximum acoustic radiation ($\theta = 150^o$ from the upstream). The flapping effect term is dominant relatively close to the jet and is commensurate with the axisymmetric modal energy. Further out along the shallow angle direction, clear differences emerge between the two jets. While the relative importance of the flapping term decays rapidly for the $AR = 4$ jet, it remains a dominant term for the $AR = 8$ jet accounting for approximately 10% of the axisymmetric modal energy.

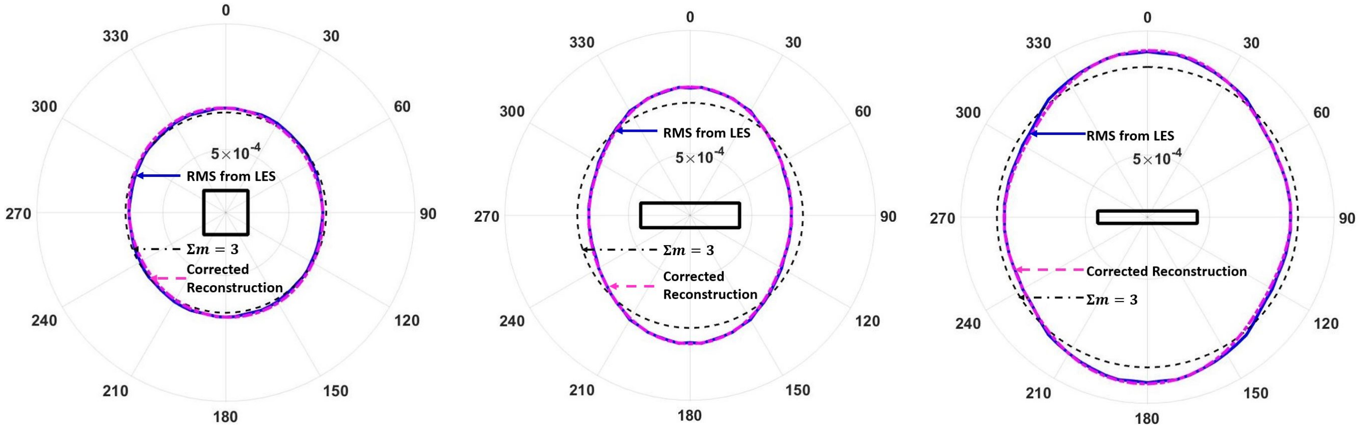

(a) $AR = 1$ (b) $AR = 4$ (c) $AR = 8$

FIG. 19: Comparison of the nearfield acoustic intensity reconstruction without (equation 27) and with (equation 29) a consideration of the terms representing the inhomogeneity of the non-axisymmetric jets

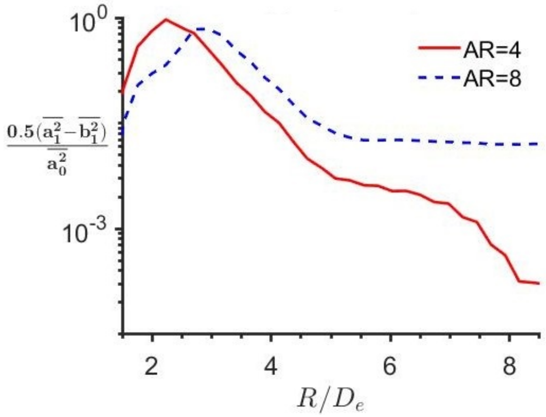

FIG. 20: Comparison of the relative importance of preferential flapping motions in rectangular jets along the direction of peak acoustic radiation

## VIII. CONCLUSIONS

The advantages of azimuthal Fourier decomposition, whose benefits are well established for circular jet analysis, are evaluated for rectangular jets using Large Eddy Simulations and by projecting the fluctuations on a cylindrical coordinate system. A related goal is to examine the effectiveness of such a decomposition for nearfield acoustic reconstruction with a reduced order model. The three $AR$ chosen, $AR = 1$, $AR = 4$, and $AR = 8$ incorporate several flow phenomena pertinent to rectangular jets, including rapid transition to axisymmetric cross section ($AR = 1$), axis-switching ($AR = 4$), and azimuthal non-uniformity in farfield acoustic radiation ($AR = 8$). They also contain other important features such as potential core length reduction and jet spreading rate increase with $AR$.

The utility of azimuthal Fourier decomposition is examined by replacing the commonly used complex exponential ansatz with separate coefficients for sine and cosine modes; this provides a more convenient representation of features that do not display axisymmetric behavior. Fluctuations from all $AR$ jets show rapid declines in higher azimuthal mode content; as such, the convergence observed in circular jet data remains valid for rectangular jets. Even for the $AR = 8$ jet, the use of the three leading azimuthal wavenumbers yields relatively small error in the instantaneous fluctuation field as well as volume integrated measures. Consistent with circular jet modeling, the acoustic field from a fluid-thermodynamic decomposition exhibits lower rank behavior than pressure.

The primary differences in plume evolution between rectangular and circular jets are evident in the first azimuthal mode, whose sine and cosine coefficients contain the qualitatively distinct processes on the major and minor axis planes of the rectangular jets. Further, a comparison of the spatial variation of the RMS acoustic fluctuation magnitudes of the individual azimuthal modes indicates that the streamwise extent reduces with increase in the $AR$, consistent with a similar trend in the length of the potential core found in the corresponding mean flow fields.

Finally, the loss of azimuthal homogeneity in rectangular jets and the non-axisymmetric RMS fluctuations is analyzed with a generalized expression for second order statistics in terms of the azimuthal modal energies. This expression highlights, as a special case, the appreciable simplification afforded by an azimuthal homogeneity, as in circular jets. For rectangular jets, significant simplifications are also shown to be possible by incorporating their two-fold mirror symmetry. By analysing individual terms, preferential flapping along the minor axis direction is confirmed as the dominant effect in loss of axisymmetry in rectangular jets. Rectangular jet modeling is, thus, greatly aided by the rapid convergence of the fluctuation statistics in azimuthal Fourier space, as well as features of the general expression for acoustic reconstruction as a function of the individual modal energies. These findings should facilitate more advanced acoustic models for rectangular jets that leverage many of the mature techniques developed for circular jets.

## ACKNOWLEDGMENTS

This research was supported by the Office of Naval Research (Grant: N00014-17-1-2584). The opinions, findings, views, conclusions or recommendations contained herein are those of the authors and should not be interpreted as necessarily representing the official policies or endorsements, either expressed or implied, of ONR or the U.S. Government. The simulations were performed with a grant of computer time from the DoD HPCMP DSRCs at AFRL, NAVO and ERDC, and the Ohio Supercomputer Center. Some figures were made using FieldView software with licenses obtained from the Intelligent Light University Partnership Program.

## Appendix A: Constraints on Fourier Modes Due to Homogeneity

To highlight some properties associated with azimuthal homogeneity we consider a spatio-temporal function $f(\phi, t)$, with $\phi$ being periodic over $2\pi$. $f(\phi, t)$ may be written as a Fourier series:

$$f(\phi,t) = a_0(t) + \sum_{m=1}^{\infty} a_m(t)\cos(m\phi) + b_m(t)\sin(m\phi) \tag{A1}$$

Rapid convergence of the instantaneous statistics in the Fourier basis allows simplification by truncation of the series beyond the dominant leading terms. If only the axisymmetric ($m = 0$) and first azimuthal ($m = 1$) modes are considered, we have:

$$f(\phi,t) = a_0(t) + a_1(t)\cos(\phi) + b_1(t)\sin(\phi) \tag{A2}$$

Azimuthal homogeneity imposes constraints on the Fourier coefficients $a_m$ and $b_m$ and may be written as:

$$\overline{f(\phi_1,t)f(\phi_2,t)} = g(\phi_1 - \phi_2) \tag{A3}$$

Here, $\overline{(.)}$ refers to an averaging operation in time. Substituting the truncated Fourier series (equation A2) in the expression for the cross-correlation leads to:

$$\begin{aligned}\overline{f(\phi_1,t)f(\phi_2,t)} &= \overline{a_0^2} + \overline{a_1^2}\cos(\phi_1)\cos(\phi_2) + \overline{b_1^2}\sin(\phi_1)\sin(\phi_2)\\ &+\overline{a_0a_1}(\cos\phi_1 + \cos\phi_2) + \overline{a_0b_1}(\sin\phi_1 + \sin\phi_2) + \overline{a_1b_1}(\sin\phi_1\cos\phi_2 + \sin\phi_2\cos\phi_1)\end{aligned}$$

The resulting expression is arranged such that terms involving the product of similar Fourier modes appear on the first line and are referred to as self-terms (S). The terms on the second line represent interactions between Fourier modes and are, thus, referred to as cross terms. The self terms may be further simplified by adding and subtracting two terms, namely $\frac{\overline{a_1^2}}{2}\sin(\phi_1)\sin(\phi_2)$ and $\frac{\overline{b_1^2}}{2}\cos(\phi_1)\cos(\phi_2)$ to read:

$$\begin{gathered}\mathbf{S} = \overline{a_0^2} + \overline{a_1^2}\cos(\phi_1)\cos(\phi_2) + \overline{b_1^2}\sin(\phi_1)\sin(\phi_2) =\\ \overline{a_0^2} + \frac{\overline{a_1^2} + \overline{b_1^2}}{2}\Bigg[\cos(\phi_1)\cos(\phi_2) + \sin(\phi_1)\sin(\phi_2)\Bigg] + \frac{\overline{a_1^2} - \overline{b_1^2}}{2}\Bigg[\cos(\phi_1)\cos(\phi_2) - \sin(\phi_1)\sin(\phi_2)\Bigg]\end{gathered}$$

which may be simplified to:

$$\mathbf{S} = \overline{a_0^2} + \frac{\overline{a_1^2} + \overline{b_1^2}}{2}\cos(\phi_1 - \phi_2) + \frac{\overline{a_1^2} - \overline{b_1^2}}{2}\cos(\phi_1 + \phi_2)$$

On substituting the above form of the self-terms in the expression for the cross-correlation matrix, the following expression is obtained:

$$
\begin{aligned}
&\overline{f(\phi_1,t)f(\phi_2,t)} = \overline{a_0^2} + \frac{\overline{a_1^2}+\overline{b_1^2}}{2}\cos{(\phi_1-\phi_2)}\\
&+\frac{\overline{a_1^2}-\overline{b_1^2}}{2}\cos{(\phi_1+\phi_2)} + \overline{a_0 a_1}(\cos\phi_1+\cos\phi_2)\\
&+\overline{a_0 b_1}(\sin\phi_1+\sin\phi_2) + \overline{a_1 b_1}(\sin\phi_1\cos\phi_2+\sin\phi_2\cos\phi_1)
\end{aligned}
$$

The right hand side of the above expression is a function of angular separation $(\phi_1-\phi_2)$ alone, all terms on the second and third line are zero for all values of $\phi_1$ and $\phi_2$. This leads to two important classes of constraints on the individual Fourier coefficients ($a_0$, $a_1$ and $b_1$):

- $\overline{a_m^2} = \overline{b_m^2}$ - The sine and cosine coefficients of a given wavenumber have equal RMS
- $\overline{a_m a_n} = \overline{b_m b_n} = \overline{a_m b_n} = 0$ - The individual azimuthal Fourier coefficients are mutually uncorrelated

Under these conditions, the cross-correlation function is given by:

$$
\overline{f(\phi_1,t)f(\phi_2,t)} = \overline{a_0^2} + \frac{\overline{a_1^2}+\overline{b_1^2}}{2}\cos{(\phi_1-\phi_2)}
$$

and thus also satisfies the condition for circumferential isotropy, in that it is independent of the sign of the angular displacement [14]. Thus $\overline{f(\phi_1,t)f(\phi_2,t)} = g(\phi_1-\phi_2) = g(\phi_2-\phi_1)$.

The constraints imposed on individual Fourier coefficients due to the statistical homogeneity also significantly simplifies the reconstruction of the RMS fluctuations using Fourier modes. In general, the RMS of $f(\phi,t)$ in terms of the three leading Fourier coefficients is given by:

$$
\begin{aligned}
\overline{f^2(\phi,t)} &= \overline{a_0^2} + \overline{a_1^2}\cos^2\phi + \overline{b_1^2}\sin^2\phi + \overline{a_2^2}\cos^2 2\phi + \overline{b_2^2}\sin^2 2\phi\\
&+ 2\overline{a_0 a_1}\cos\phi + 2\overline{a_0 b_1}\sin\phi + 2\overline{a_0 a_2}\cos 2\phi + 2\overline{a_0 b_2}\sin 2\phi\\
&+ \overline{a_1 b_1}\sin\phi\cos\phi + \overline{a_1 a_2}\cos\phi\cos 2\phi + \overline{a_1 b_2}\cos\phi\sin 2\phi\\
&+ \overline{b_1 a_2}\sin\phi\cos 2\phi + \overline{b_1 b_2}\cos\phi\sin 2\phi + \overline{a_2 b_2}\cos 2\phi\sin 2\phi
\end{aligned} \tag{A4}
$$

The terms on the RHS of the above relation can again be split into self terms consisting of contributions from the sine and cosine coefficients of the same azimuthal mode number (first two lines) and cross terms representing modal interactions. Using trigonometric identities, the self terms in the above expression can be rearranged to:

$$
\begin{aligned}
\overline{f^2(\phi,t)} &= \overline{a_0^2} + \frac{\overline{a_1^2}+\overline{b_1^2}}{2} + \frac{\overline{a_2^2}+\overline{b_2^2}}{2}\\
&+ \frac{\overline{a_1^2}-\overline{b_1^2}}{2}\cos 2\phi + \frac{\overline{a_2^2}-\overline{b_2^2}}{2}\cos 4\phi\\
&+ 2\overline{a_0 a_1}\cos\phi + 2\overline{a_0 b_1}\sin\phi + 2\overline{a_0 a_2}\cos 2\phi + 2\overline{a_0 b_2}\sin 2\phi\\
&+ 2\overline{a_1 b_1}\sin\phi\cos\phi + 2\overline{a_1 a_2}\cos\phi\cos 2\phi + 2\overline{a_1 b_2}\cos\phi\sin 2\phi\\
&+ 2\overline{b_1 a_2}\sin\phi\cos 2\phi + 2\overline{b_1 b_2}\cos\phi\sin 2\phi + 2\overline{a_2 b_2}\cos 2\phi\sin 2\phi
\end{aligned} \tag{A5}
$$

This form facilitates an understanding of the physical mechanisms that contribute to an asymmetry, that is, a dependence on $\phi$. All the terms in this expression, apart from those on the first line, represent physical processes that are a direct result of the inhomogeneity of the statistics in the azimuthal direction.

The constraints due to homogeneity derived previously simplify the expression for the RMS to:

$$
\overline{f^2(\phi,t)} = \overline{a_0^2} + \frac{\overline{a_1^2}+\overline{b_1^2}}{2} + \frac{\overline{a_2^2}+\overline{b_2^2}}{2} \tag{A6}
$$

Thus, the RMS of the function is given as the summation of the contributions of the individual azimuthal modes in the homogeneous direction, and is independent of the angular position $\phi$. This crucial result implies that azimuthal invariance of the RMS holds no matter how many individual azimuthal modes are retained.

---

[1] C. K. W. Tam, Supersonic jet noise, Annual review of fluid mechanics **27**, 17 (1995).

[2] P. Jordan and T. Colonius, Wave packets and turbulent jet noise, Annual review of fluid mechanics **45**, 173 (2013).

[3] T. Suzuki, A review of diagnostic studies on jet-noise sources and generation mechanisms of subsonically convecting jets, Fluid Dynamics Research **42**, 014001 (2010).

[4] G. Raman, P. Panickar, and K. Chelliah, Aeroacoustics of twin supersonic jets: a review, International Journal of Aeroacoustics **11**, 957 (2012).

[5] C. Bailly and K. Fujii, High-speed jet noise, Mechanical Engineering Reviews **3**, 15 (2016).

[6] J. B. Freund and T. Colonius, Pod analysis of sound generation by a turbulent jet, in *40th AIAA Aerospace Sciences Meeting and Exhibit 2002* (2002).

[7] O. T. Schmidt, A. Towne, G. Rigas, T. Colonius, and G. A. Brès, Spectral analysis of jet turbulence, Journal of Fluid Mechanics **855**, 953 (2018).

[8] K. Gudmundsson and T. Colonius, Instability wave models for the near-field fluctuations of turbulent jets, Journal of Fluid Mechanics **689**, 97 (2011).

[9] E. Pickering, G. Rigas, O. T. Schmidt, D. Sipp, and T. Colonius, Optimal eddy viscosity for resolvent-based models of coherent structures in turbulent jets, arXiv preprint arXiv:2005.10964 (2020).

[10] A. V. G. Cavalieri, P. Jordan, and L. Lesshafft, Wave-packet models for jet dynamics and sound radiation, Applied Mechanics Reviews **71**, 020802 (2019).

[11] R. Reba, S. Narayanan, and T. Colonius, Wave-packet models for large-scale mixing noise, International Journal of Aeroacoustics **9**, 533 (2010).

[12] Y. B. Baqui, A. Agarwal, A. V. G. Cavalieri, and S. Sinayoko, A coherence-matched linear source mechanism for subsonic jet noise, Journal of Fluid Mechanics **776**, 235 (2015).

[13] D. Papamoschou, Wavepacket modeling of the jet noise source, International Journal of Aeroacoustics **17**, 52 (2018).

[14] A. Michalke and H. V. Fuchs, On turbulence and noise of an axisymmetric shear flow, Journal of Fluid Mechanics **70**, 179 (1975).

[15] H. Vold, P. Shah, P. Morris, Y. Du, and D. Papamoschou, Axisymmetry and azimuthal modes in jet noise, in *18th AIAA/CEAS Aeroacoustics Conference (33rd AIAA Aeroacoustics Conference)* (2012) p. 2214.

[16] D. G. Crighton and M. Gaster, Stability of slowly diverging jet flow, Journal of Fluid Mechanics **77**, 397 (1976).

[17] F. C. Lajús, A. Sinha, A. V. G. Cavalieri, C. J. Deschamps, and T. Colonius, Spatial stability analysis of subsonic corrugated jets, Journal of Fluid Mechanics **876**, 766 (2019).

[18] A. Michalke, *A wave model for sound generation in circular jets* (Dt. Forschungs-u. Versuchsanstalt für Luft-u. Raumfahrt, Institut für , 1970).

[19] A. V. G. Cavalieri, P. Jordan, T. Colonius, and Y. Gervais, Axisymmetric superdirectivity in subsonic jets, Journal of fluid Mechanics **704**, 388 (2012).

[20] A. Sinha, D. Rodríguez, G. A. Brès, and T. Colonius, Wavepacket models for supersonic jet noise, Journal of Fluid Mechanics **742**, 71 (2014).

[21] S. C. Crow, Acoustic gain of a turbulent jet, in *Phys. Soc. Meeting, Univ. Colorado, Boulder, paper IE*, Vol. 6 (1972).

[22] V. Jaunet, P. Jordan, and A. V. G. Cavalieri, Two-point coherence of wave packets in turbulent jets, Physical Review Fluids **2**, 024604 (2017).

[23] F. F. Grinstein, Vortex dynamics and entrainment in rectangular free jets, Journal of Fluid Mechanics **437**, 69 (2001).

[24] E. J. Gutmark and F. F. Grinstein, Flow control with noncircular jets, Annual review of fluid mechanics **31**, 239 (1999).

[25] N. Chen and H. Yu, Mechanism of axis switching in low aspect-ratio rectangular jets, Computers & Mathematics with applications **67**, 437 (2014).

[26] K. B. M. Q. Zaman, Axis switching and spreading of an asymmetric jet: the role of coherent structure dynamics, Journal of Fluid Mechanics **316**, 1 (1996).

[27] C. Shih, A. Krothapalli, and S. Gogineni, Experimental observations of instability modes in a rectangular jet, AIAA journal **30**, 2388 (1992).

[28] E. Gutmark, K. C. Schadow, and C. J. Bicker, Near acoustic field and shock structure of rectangular supersonic jets, AIAA journal **28**, 1163 (1990).

[29] F. Hussain and H. S. Husain, Elliptic jets. part 1. characteristics of unexcited and excited jets, Journal of Fluid Mechanics **208**, 257 (1989).

[30] F. F. Grinstein, Self-induced vortex ring dynamics in subsonic rectangular jets, Physics of Fluids **7**, 2519 (1995).

[31] J. Bridges, Acoustic measurements of rectangular nozzles with bevel, in *18th AIAA/CEAS Aeroacoustics Conference (33rd AIAA Aeroacoustics Conference)* (2012) p. 2252.

[32] J. Veltin and D. McLaughlin, Flow field and acoustic measurements of rectangular supersonic jets, in *47th AIAA Aerospace Sciences Meeting including The New Horizons Forum and Aerospace Exposition* (2009) p. 19.

[33] N. S. Heeb, P. M. Sanchez, E. J. Gutmark, and K. Kailasanath, Investigation of the noise from a rectangular supersonic jet, in *19th AIAA/CEAS Aeroacoustics Conference* (2013) p. 2239.

[34] C. K. W. Tam, Influence of nozzle geometry on the noise of high-speed jets, AIAA journal **36**, 1396 (1998).

[35] K. W. Kinzie and D. K. McLaughlin, Azimuthal mode measurements of elliptic jets, Physics of Fluids **9**, 2000 (1997).

[36] C. K. W. Tam and A. T. Thies, Instability of rectangular jets, Journal of Fluid Mechanics **248**, 425 (1993).

[37] S. Chakrabarti, D. V. Gaitonde, and S. Unnikrishnan, The dynamics of azimuthal modes in rectangular jets, in *AIAA AVIATION 2020 FORUM* (2020) p. 3000.

[38] P. E. Doak, Momentum potential theory of energy flux carried by momentum fluctuations, Journal of sound and vibration **131**, 67 (1989).

[39] S. Unnikrishnan, A. V. G. Cavalieri, and D. V. Gaitonde, Acoustically informed statistics for wave-packet models, AIAA

Journal **57**, 2421 (2019).

[40] D. Anderson, J. C. Tannehill, and R. H. Pletcher, *Computational fluid mechanics and heat transfer* (CRC Press, 2016).

[41] M. Vinokur, An analysis of finite-difference and finite-volume formulations of conservation laws, Journal of computational physics **81**, 1 (1989).

[42] M. Samimy, J. H. Kim, M. Kearney-Fischer, and A. Sinha, Acoustic and flow fields of an excited high reynolds number axisymmetric supersonic jet, Journal of Fluid Mechanics **656**, 507 (2010).

[43] M. Samimy, J. H. Kim, J. Kastner, I. Adamovich, and Y. Utkin, Active control of high-speed and high-reynolds-number jets using plasma actuators, Journal of Fluid Mechanics **578**, 305 (2007).

[44] J. Hileman and M. Samimy, Turbulence structures and the acoustic far field of a mach 1.3 jet, AIAA journal **39**, 1716 (2001).

[45] D. V. Gaitonde, Analysis of the near field in a plasma-actuator-controlled supersonic jet, Journal of Propulsion and Power **28**, 281 (2012).

[46] D. V. Gaitonde and M. Samimy, Coherent structures in plasma-actuator controlled supersonic jets: Axisymmetric and mixed azimuthal modes, Physics of Fluids **23**, 095104 (2011).

[47] R. Speth and D. V. Gaitonde, Parametric study of a mach 1.3 cold jet excited by the flapping mode using plasma actuators, Computers & Fluids **84**, 16 (2013).

[48] S. Unnikrishnan and D. V. Gaitonde, Acoustic, hydrodynamic and thermal modes in a supersonic cold jet, Journal of Fluid Mechanics **800**, 387 (2016).

[49] K. B. M. Q. Zaman, Effect of initial condition on subsonic jet noise, AIAA journal **23**, 1370 (1985).

[50] G. A. Brès, P. Jordan, V. Jaunet, M. Le Rallic, A. V. G. Cavalieri, A. Towne, S. K. Lele, T. Colonius, and O. T. Schmidt, Importance of the nozzle-exit boundary-layer state in subsonic turbulent jets, Journal of Fluid Mechanics **851**, 83 (2018).

[51] A. Karon and K. Ahuja, Effect of nozzle-exit boundary layer on jet noise, in *51st AIAA Aerospace Sciences Meeting including the New Horizons Forum and Aerospace Exposition* (2013) p. 615.

[52] D. Whitfield, Three-dimensional unsteady euler equations solution using flux vector splitting, in *17th Fluid Dynamics, Plasma Dynamics, and Lasers Conference* (1984) p. 1552.

[53] P. L. Roe, Approximate riemann solvers, parameter vectors, and difference schemes, Journal of Computational Physics **43**, 357 (1981).

[54] J. H. Morrison, Flux difference split scheme for turbulent transport equations. 1990, AIAA Paper , 90.

[55] T. H. Pulliam and D. S. Chaussee, A diagonal form of an implicit approximate-factorization algorithm, Journal of Computational Physics **39**, 347 (1981).

[56] S. Chakrabarti, C. M. Stack, S. Unnikrishnan, D. V. Gaitonde, F. Baier, A. Karnam, and E. J. Gutmark, On the turbulence statistics of a hot, overexpanded rectangular jet, in *AIAA Scitech 2020 Forum* (2020) p. 0819.

[57] F. F. Grinstein and K. Kailasanath, Three-dimensional numerical simulations of unsteady reactive square jets, Combustion and Flame **100**, 2 (1995).

[58] D. J. Bodony and S. K. Lele, On using large-eddy simulation for the prediction of noise from cold and heated turbulent jets, Physics of Fluids **17**, 085103 (2005).

[59] A. Krothapalli, D. Baganoff, and K. Karamcheti, On the mixing of a rectangular jet, Journal of Fluid Mechanics **107**, 201 (1981).

[60] P. Di Francescantonio, A new boundary integral formulation for the prediction of sound radiation, Journal of Sound and Vibration **202**, 491 (1997).

[61] S. Mendez, M. Shoeybi, S. K. Lele, and P. Moin, On the use of the Ffowcs Williams-Hawkings equation to predict far-field jet noise from large-eddy simulations, International Journal of Aeroacoustics **12**, 1 (2013).

[62] R. A. Kantola, Noise characteristics of heated high velocity rectangular jets, Journal of Sound and Vibration **64**, 277 (1979).

[63] I. A. Maia, P. Jordan, A. V. G. Cavalieri, and V. Jaunet, Two-point wavepacket modelling of jet noise, Proceedings of the Royal Society A **475**, 20190199 (2019).

[64] M. E. Goldstein, On identifying the true sources of aerodynamic sound, Journal of Fluid Mechanics **526**, 337 (2005).

[65] C. E. Tinney and P. Jordan, The near pressure field of co-axial subsonic jets, Journal of Fluid Mechanics **611**, 175 (2008).

[66] R. E. A. Arndt, D. F. Long, and M. N. Glauser, The proper orthogonal decomposition of pressure fluctuations surrounding a turbulent jet, Journal of Fluid Mechanics  (1997).

[67] C. Bogey, S. Barré, V. Fleury, C. Bailly, and D. Juvé, Experimental study of the spectral properties of near-field and far-field jet noise, International Journal of Aeroacoustics **6**, 73 (2007).

[68] S. Unnikrishnan and D. V. Gaitonde, Interactions between vortical, acoustic and thermal components during hypersonic transition, Journal of Fluid Mechanics **868**, 611 (2019).

[69] D. G. Crighton, Instability of an elliptic jet, Journal of Fluid Mechanics **59**, 665 (1973).

[70] A. V. G. Cavalieri, D. Rodríguez, P. Jordan, T. Colonius, and Y. Gervais, Wavepackets in the velocity field of turbulent jets, Journal of Fluid Mechanics **730**, 559 (2013).

[71] G. A. Faranosov, I. V. Belyaev, V. F. Kopiev, M. Y. Zaytsev, A. A. Aleksentsev, Y. V. Bersenev, V. A. Chursin, and T. A. Viskova, Adaptation of the azimuthal decomposition technique to jet noise measurements in full-scale tests, AIAA Journal **55**, 572 (2017).

[72] S. Unnikrishnan, *Jet noise source localization and identification*, Ph.D. thesis, The Ohio State University (2017).